

SCALABLE SPATIAL POINT PROCESS MODELS FOR FORENSIC FOOTWEAR ANALYSIS

BY ALOKESH MANNA^a, NEIL SPENCER^b AND DIPAK K. DEY^c

UNIVERSITY OF CONNECTICUT, DEPARTMENT OF STATISTICS, STORRS, CT 06269, UNITED STATES. ^aALOKESH.MANNA@UCONN.EDU,
^bNEIL.SPENCER@UCONN.EDU, ^cDIPAK.DEY@UCONN.EDU

Shoe print evidence recovered from crime scenes plays a key role in forensic investigations. By examining shoe prints, investigators can determine details of the footwear worn by suspects. However, establishing that a suspect's shoes match the make and model of a crime scene print may not be sufficient. Typically, thousands of shoes of the same size, make, and model are manufactured, any of which could be responsible for the print. Accordingly, a popular approach used by investigators is to examine the print for signs of "accidentals" i.e., cuts, scrapes, and other features that accumulate on shoe soles after purchase due to wear. While some patterns of accidentals are common on certain types of shoes, others are highly distinctive, potentially distinguishing the suspect's shoe from all others. Quantifying the rarity of a pattern is thus essential to accurately measuring the strength of forensic evidence. In this study, we address this task by developing a hierarchical Bayesian model. Our improvement over existing methods primarily stems from two advancements. First, we frame our approach in terms of a latent Gaussian model, thus enabling inference to be efficiently scaled to large collections of annotated shoe prints via integrated nested Laplace approximations. Secondly, we incorporate spatially varying coefficients to model the relationship between shoes' tread patterns and accidental locations. We demonstrate these improvements through superior performance on held-out data, which enhances accuracy and reliability in forensic shoe print analysis.

1. Introduction

Footwear impressions are a common form of forensic evidence, useful for both suspect identification and crime scene reconstruction (Bodziak, 2017). Traditionally, analysis and courtroom testimony regarding footwear evidence has relied almost exclusively on the expertise of trained examiners. However, recent reports on forensic science have emphasized the need for methods that are data-driven and empirically validated (Council et al., 2009; Holdren et al., 2016). In response, researchers are developing statistical methods for footwear analysis (Srihari, 2011; Srihari and Tang, 2014; Shor et al., 2018; Spencer and Murray, 2020; Venkatasubramanian et al., 2021; Shafique et al., 2023), and curating databases to train and evaluate these methods (ChoChół and Świątek, 2012; Yekutieli et al., 2012; Kortylewski, Albrecht and Vetter, 2014; Speir et al., 2016; Lin, DeBat and Speir, 2022; Pasquier, 2023)

One key focus in footwear analysis is the study of accidentals, or randomly acquired characteristics (RACs). These are the cuts, holes, and embedded materials that accumulate on shoe outsoles through use. Because thousands of identical shoes are manufactured, a suspect's shoe typically cannot be definitively linked to a print based solely on a tread design match. Instead, examiners rely on accidentals to distinguish between shoes with matching tread design.

Nevertheless, accidentals are not perfectly distinctive. Certain shoes may be especially prone to accidentals in particular regions, increasing the likelihood that two shoes exhibit patterns of accidentals that coincidentally match. Consequently, it is important to quantify the

Keywords and phrases: Forensic Data Analysis, Hierarchical Bayesian Model, Spatial point process, Latent Gaussian Models, Image analysis, Sparse data modeling, Gaussian Process.

probability of such coincidences when considering the correspondence of a suspect's shoe with a crime scene print. Following the calls of [Council et al. \(2009\)](#); [Holdren et al. \(2016\)](#), these probability estimates should be grounded in relevant data and empirically validated.

How should one go about this? Ideally, for a specific shoe print, one would analyze the accidental configurations of many shoes of that same make and model, estimating a probability distribution over all possible accidental configurations. However, such data are unavailable outside a few special cases ([Champod, Voisard and Girod \(2000\)](#), [Frachtenicht, Herzig and Blackledge \(2002\)](#), [Adair et al. \(2007\)](#), [Wilson \(2012\)](#)). Indeed, datasets consisting of worn shoes with annotated accidentals are scarce in general. Existing resources consist largely of convenience samples that span a wide range of outsole designs with little replication. The two most prominent examples in the literature are the JESA database ([Yekutieli et al., 2012](#)) and the West Virginia University (WVU) database ([Speir et al., 2016](#)). JESA was collected by the Israeli police, comprising 386 worn shoes from forensic casework. The WVU database includes an opportunistic sample of 1,300 shoes from the United States.

Although not perfectly suited for estimating the shoe-specific distribution of accidentals, models based on these collections have nonetheless shown promising results. Notably, [Spencer and Murray \(2020\)](#) developed a Bayesian hierarchical point process regression framework to pool information across shoes in the JESA database. Their model, tailored to capture both spatial trends in accidental locations and the impact of the shape of the shoe sole's contact surface, substantially outperformed more traditional baselines ([Stone \(2006\)](#)). It is worth noting that such improvements in model accuracy can translate into large differences in estimated random match probabilities, substantially impacting the strength of the conclusions drawn. Related contributions, such as those by [Speir et al. \(2016\)](#); [Kaplan-Damary et al. \(2022\)](#), further validate the promise of data-driven methods.

Yet these existing approaches face important limitations. The model of [Spencer and Murray \(2020\)](#) was constrained by the relatively small size of the JESA database, and the computational challenges of fitting bespoke Bayesian hierarchical models. Expanding datasets such as the WVU database demand methods that are both expressive and scalable. Simpler aggregate models, such as those of [Kaplan-Damary et al. \(2022\)](#) or [Speir et al. \(2016\)](#), scale to larger datasets, but lack the flexibility to explicitly tailor accidental distributions to specific outsoles.

Accordingly, the goal of this study is to develop a model for accidental configurations that is both expressive and computationally scalable. Building on the point process problem formulation of [Spencer and Murray \(2020\)](#), we re-frame this task as fitting a latent Gaussian spatial point process model. This approach enables fast approximate Bayesian inference via integrated nested Laplace approximations (INLA, [Rue et al. \(2017\)](#)), allowing for more sophisticated models that scale easily to the larger WVU dataset and any future datasets collected. Our model incorporates spatially varying coefficients for outsole contact-surface features, which not only yield interpretable results but also improve performance over existing methods by capturing nonlinear relationships between features and accidentals.

We have structured the remainder of the paper as follows. In Section 2.1, we provide a detailed description of the problem, followed by some practical considerations in Section 2.2, and a literature survey in Section 2.3. The available data from WVU is described in Section 3. In Section 4, we present the model formulation as a latent Gaussian Cox process. The computational procedure for parameter inference using integrated nested Laplace approximation and the choice of the priors are elaborated in Section 5. In Section 6, we discuss the fit and results of the model, providing insight on where accidentals are likely to occur, given a shoe's specific tread pattern. To assess predictive performance and compare different methods, we introduce the evaluation metrics in Section 7, and demonstrate the superior performance of the proposed model over competing methods. Finally, in Section 8, we summarize the key findings, highlighting the novelty and potential contributions of this work. Additional detailed calculations and descriptions are provided in the supplementary material.

2. Background

2.1. Description of Problem

As detailed in [Spencer and Murray \(2020\)](#), the probability that a shoe coincidentally matches the accidentals of a print can be quantified using accidental-based random match probabilities. Generally, random match probabilities represent the chance that a randomly selected shoe from a relevant population (e.g., all shoes of a given type within a city) would produce a print consistent with the considered features (e.g. accidentals).

In forensic investigations, accidentals are typically compared only after establishing a match in both class characteristics (the size, make, and model of the shoe), and any distinctive general wear patterns (e.g. deterioration of an entire region of the outsole's tread). Accordingly, accidental-based random match probabilities are defined as conditional on established agreement in both class characteristics and general wear.

To formalize this concept, consider the framework presented in [Spencer and Murray \(2020\)](#), adapted from [Skerrett, Neumann and Mateos-Garcia \(2011\)](#). Let y denote a shoe print, with y_M , y_W , and y_V , respectively denoting its class characteristics, general wear, and accidentals. Similarly, let s_M , s_W , s_V denote these features for a shoe s . Finally, let \mathbb{A} denote the relevant population of shoes, and let $s \sim \mathbb{A}$ denote a shoe drawn uniformly at random from the set \mathbb{A} .

Within this notational framework, the accidental-based random match probability rmp_V of the shoe s and print y is given by:

$$rmp_V := \mathbb{P}(y_V \equiv s_V \mid s \sim A_y), \text{ where } A_y := \{s \in \mathbb{A} : y_M \equiv s_M, y_W \equiv s_W\}.$$

Here, $y_i \equiv s_i$ denotes feature $i \in \{V, M, W\}$ on shoe s being consistent with that of the print y .

It is worth noting that our use of ‘consistent with’ (\equiv) language instead of the stricter ‘equal to’ ($=$) stems from inherent challenges of footwear comparison. For class characteristics, two shoes of slightly different models or sizes (e.g., off by a half size) can produce prints with practically indistinguishable tread patterns. It is thus more practical to consider all shoes with consistent tread patterns (up to some tolerance measure) rather than shoes that match the class characteristics exactly. The same goes for general wear; wear tends to present slightly differently between prints, especially if time has elapsed between comparisons. Finally, for accidentals, their spatial coordinates cannot be measured with arbitrary precision ([Shor et al. \(2018\)](#)). Moreover, depending on the quality of the print y , not all accidentals present on the source shoe s may be detectable. To account for each of these challenges, the tolerance measures used to define \equiv for each feature should be context-specific, depending on the quality and medium of the crime scene print, as well as the precision of the measurement tools.

Bringing this together, rmp_V quantifies the chance that the accidentals s_V on a randomly chosen shoe are consistent (up to some tolerance measure) with those of print y , given that its class characteristics s_M and general wear s_W are consistent with y . In this work, we avoid a specific choice of tolerance measures, instead directly modeling $s_V \mid s_M, s_W$ —the distribution of a shoe's spatial configuration of accidentals conditional on its class characteristics and wear. For any chosen tolerance measure, this distribution allows rmp_V to be evaluated.

Because s_M and s_W are not directly available in existing databases, we follow [Spencer and Murray \(2020\)](#) and use the “contact surface” C_s of shoe s as a practical proxy, thus re-framing the problem as modeling the distribution $s_V \mid C_s$. Here, the contact surface refers to an image of a high-quality sample print obtained using the shoe's outsole (e.g. Figure 2a). Such images, along with corresponding accidental coordinates, are routinely collected for shoes in forensic footwear investigations, and are available for all shoes in both the JESA and WVU databases. We elaborate on this point in Section 3.1.

2.2. Practical Considerations

Recall that the JESA and WVU databases consist of convenience samples of shoes exhibiting a wide range of outsole designs, with few repeats of the same contact surface. Thus, it is not practical to infer the distribution $p(s_V | C_s)$ based only on shoes with contact surface C_s .

Instead, it is helpful to combine information across a variety of accidental-contact surface pairs (s_V, C_s) within a given database, improving statistical performance by capturing commonalities between them. This essentially frames the $s_V | C_s$ distribution estimation problem as a spatial point pattern regression task, where the accidental locations s_V are the random spatial point pattern (the response), and the contact surfaces C_s play the role of the covariates.

2.3. Previous Work

As a preliminary step toward computing accidental-based random match probabilities, [Stone \(2006\)](#) proposed a simple hypothetical probability model for accidentals, assuming a uniform distribution for their locations on the shoe's outsole. Rather than being data-informed, these simple assumptions were made out of mathematical convenience, intended to illustrate how random match probabilities could, in principle, be quantified objectively. [Stone \(2006\)](#) claims the uniform assumption is a conservative choice, but this is not the case. The uniform distribution has the maximum entropy among continuous distributions, so it will generally underestimate random match probabilities whenever the true distribution is non-uniform. This leads to overconfident conclusions.

Subsequent studies have empirically examined the validity of the uniformity assumption. Based on a preliminary analysis of the JESA database, [Wiesner et al. \(2020\)](#) suggested that uniformity might be reasonable. However, this conclusion was later rejected by [Kaplan-Damary et al. \(2022\)](#) via a formal hypothesis test on the same data. Concurrently, [Richetelli and Speir \(2022\)](#) analyzed the WVU database and also found strong evidence of non-uniformity. Finally, [Spencer and Murray \(2020\)](#) demonstrated that data-driven, non-uniform models consistently outperform the uniform baseline when evaluated on held-out data from the JESA database.

Moving beyond uniform models, most recent work has focused on data-driven approaches that pool information across convenience samples of accidentally annotated contact surfaces, such as those in the JESA or WVU databases. With the exception of [Spencer and Murray \(2020\)](#), these studies follow a broadly similar two-step strategy:

1. Registration: Align all shoes to a common coordinate system based on a registration criterion.
2. Aggregation: Combine the aligned accidental locations to estimate a shared spatial distribution across shoes.

[Yekutieli et al. \(2012\)](#), [Wiesner et al. \(2020\)](#), and [Kaplan-Damary et al. \(2022\)](#) each used the JESA database, and the following registration strategy rooted in Euclidean coordinates: (i) center the contact surface at the origin, (ii) rotate it so that its principal axis is vertical, (iii) scale to unit height, and (iv) reflect right shoes so they coincide with left shoes. These studies then differed in how they aggregated accidentals, with [Yekutieli et al. \(2012\)](#) and [Wiesner et al. \(2020\)](#) applying two-dimensional kernel density estimation, whereas [Kaplan-Damary et al. \(2022\)](#) aggregated counts within 14 expert-defined subregions of the shoe.

For the WVU database, [Speir et al. \(2016\)](#) and [Richetelli and Speir \(2022\)](#) registered shoes using polar coordinates, standardizing each shoe's accidental and contact surface locations onto a common reference outsole. This registration approach ensures alignment of the contact surface boundary across shoes, at the cost of distorting interior Euclidean distances. After registration, both studies estimated spatial accidental densities using two-dimensional histograms. In addition, [Richetelli and Speir \(2022\)](#) proposed a second model that included an

aggregated contact surface term, allowing the accidental propensity at a location to depend on the number of standardized WVU database shoes with contact surface at that coordinate.

Despite differences in implementation, all of these studies yield similar outputs: a spatial “heat map” of accidental propensity, indicating regions of the outsole that are more or less prone to accidentals. In principle, this heat map can be transformed back into the coordinate system of any given shoe, providing an estimate of $s_V | C_s$. However, a key limitation of these approaches is that, beyond being used in registration, the specific contact surface C_s of a shoe is not considered. That is, the resultant $s_V | C_s$ does not specifically depend on C_s . Even for [Richetelli and Speir \(2022\)](#), the impact of C_s is the same as the contact surface of all other shoes in the database. Hence, $s_V | C_s$ depends only very weakly on C_s , limiting the capacity to infer shoe-specific accidental distributions.

To address this limitation, [Spencer and Murray \(2020\)](#) proposed a semi-parametric hierarchical Bayesian model that directly links accidental locations to local properties of the contact surface. Their framework treats the accidentals on a shoe as a realization of a spatial Cox process, with the spatial log-intensity modeled as a sum of smooth spatial effects and covariate effects derived from the contact surface. To make inference computationally feasible, the contact surface image was coarsened and binarized, allowing the geometric configuration of tread (contact versus non-contact) of nearby pixels to enter the model as a categorical predictor. Posterior inference was conducted using a bespoke Markov chain Monte Carlo strategy, and model performance was evaluated through cross-validation on the JESA database. The results showed that direct incorporation of the contact surface yielded a substantially better fit than registration-and-aggregation approaches, underscoring the importance of modeling C_s directly to estimate $s_V | C_s$. Nevertheless, the model’s expressiveness was constrained by the small size of the JESA dataset and by the computational cost of the Bayesian inference strategy. The goal of the present manuscript is to build on this work by presenting a richer contact surface model fit to more data using a more computationally efficient inference strategy.

Before proceeding to this new work, it is worth highlighting additional work—both foundational and more recent—focusing on broader statistical issues in forensic footwear analysis. [Evett, Lambert and Buckleton \(1998\)](#) presented a Bayesian consideration of the forensic practice of individualization of evidence, along with an application to the likelihood ratio approach in forensic footwear. [Lund and Iyer \(2016\)](#), [Lund and Iyer \(2017\)](#), and [Lund and Iyer \(2022\)](#) explore similar foundational questions in greater depth, including the objectivity of forensic evidence and interpretations of uncertainty in forensic likelihood ratios.

Multiple recent works ([Richetelli et al., 2017](#); [Damary et al., 2018](#); [Richetelli, Bodziak and Speir, 2019](#); [Smale and Speir, 2023](#)) have considered the related problem of empirically assessing the distinctiveness of an individual accidental based on features such as location, shape, and type. Notably, [Smale and Speir \(2024a\)](#), [Smale and Speir \(2024b\)](#) considered this problem on realistic crime scene prints, considering prints left in blood and dust, respectively.

Another promising line of recent research has applied deep learning methods to the matching of shoeprint images, mainly addressing the problems of checking $y_M \equiv s_M$ and $y_W \equiv s_W$. One notable example is the quantitative workflow proposed by [Venkatasubramanian et al. \(2021\)](#) that computes multiple similarity scores based on outsole design, size, wear, and accidentals. Performance of such algorithms depends on accurate alignment of shoeprint images, and is therefore sensitive to registration errors. To side-step this issue, [Jang, Park and Carriquiry \(2023\)](#) proposed Shoe-MS, a deep learning technique that can successfully compare prints without the need for explicit registration, and has been shown to be effective even on degraded images ([Jang, Carriquiry and Park, 2025](#)). A key driver of the success of this technique is the use of a “Siamese” neural network to derive suitable features for comparison, a technique first proposed for shoe comparison by [Kong et al. \(2017\)](#). Other pioneering data-driven work in this area includes [Kortylewski, Albrecht and Vetter \(2014\)](#) and [Srihari and Tang \(2014\)](#).

3. Description of Data

Our analysis will focus on a large footwear database of worn shoes as collected by Dr. Jacqueline Speir's research group at West Virginia University. This database pertains to 650 shoe pairs for a total of 1,300 distinct shoes. These shoes vary on a wide range of features, including size, manufacturer, amount of wear, and outsole design. For each shoe, our investigation will primarily center on two distinct objects:

1. The laboratory generated impression (e.g., Figures 1a–1d): a high-quality sample print obtained by dusting a shoe's outsole with black powder, pressing it onto a clear polyester sheet, then scanning the sheet to obtain a moderate to high resolution grayscale image.
2. The configuration of accidental locations (e.g., Figure 1e): the coordinates of each accidental occurrence on the shoe sole image as determined by trained researchers.

Descriptions of these objects, as well as accompanying pre-processing steps and mathematical notation, follow in Sections 3.1 and 3.2 below. For additional details concerning the data source and collection methodology, see [Speir et al. \(2016\)](#), [Richetelli, Bodziak and Speir \(2019\)](#), and [Richetelli and Speir \(2022\)](#).

3.1. Shoe print Image

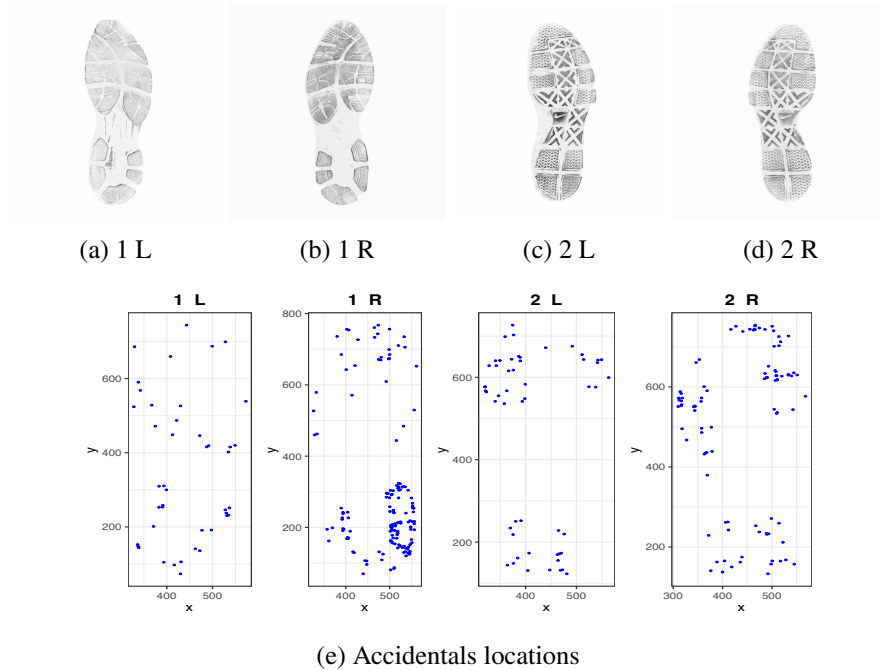
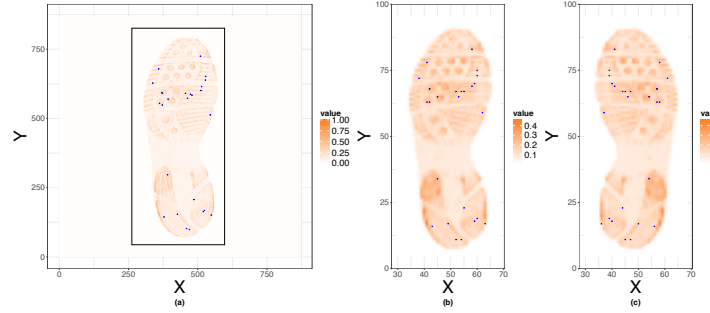


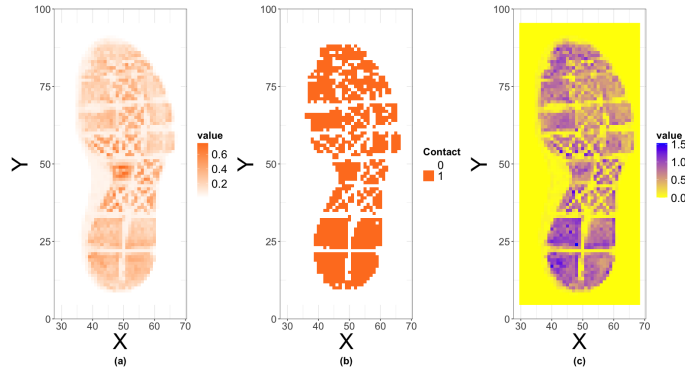
Fig 1: Four original images of shoeprints and accidental locations

3.1.1. Raw Image Processing

Figures 1a, 1b, 1c, 1d depict four example shoe print images from the WVU database ([Speir et al. \(2016\)](#)); Figures 1a and 1b show the left and right shoes comprising the first pair in the database, and 1c and 1d show the left and right shoes of the second pair.



(2a) Shoe 3 R Images: Original, Coarsened, and Reflected.



(2b) Shoe 2 Images: Coarsened, Binary, and Image Gradient.

Fig 2: Visual comparisons of contact surface transformations across two example shoes.

We initially obtained these data in a moderate to high resolution format, with each image consisting of 869×869 grayscale pixels valued over $[0, 1]$, with 0 corresponding to white and 1 corresponding to black. The images were already pre-centered and aligned so that the toe-heel orientation generally aligns with the vertical axis, and the width of the shoe with the horizontal axis. Left shoe prints were oriented to have the big toe on the left-hand side, and right shoes to have it on the right-hand side.

To render these images suitable for our modeling, additional processing steps were required. First, to allow for the direct pooling of spatial information across both left and right shoes, we followed conventions in the field (Yekutieli et al., 2012; Richeletti and Speir, 2022) and reflected right shoe images along their vertical axis to match the layout of left shoes.

Secondly, for computational efficiency, we eliminated the unnecessary white padding on the sides of the images created by their initial square shape 869×869 , considering instead the rectangular region defined by the coordinates in (262, 597) for the horizontal axis and (44, 826) for the vertical axis. These boundaries retained all shoe print pixels, resulting in 336×783 images. This resolution is excessively fine-grained for both our modeling goals and computational budget. So, we also coarsened the images, averaging the intensities across 8.7 by 8.7 patches of pixels to reduce the dimension of our final images to a resolution of 39×91 , depicted over the range $[30, 68] \times [5, 95]$. This coarser grid retains sufficient details of the tread patterns of shoes, as can be seen by comparing the original image to the coarsened version in Figure 2a.

3.1.2. Notation

The following mathematical notation helps describe how the shoe print images are incorporated into our models in Section 4. Let us first define the set of all 1300 sample shoes available as \mathcal{S} , with $|\mathcal{S}| = 1300$. We will use the notation $s \in \mathcal{S}$ when indexing over all shoes in the dataset. We will use two-dimensional Euclidean coordinates to describe the 39×91 grid defined by the processed shoe print images.

For our simplified notation, we define $\mathcal{A} := \{(x, y) : x = 1, 2, \dots, n_x, y = 1, 2, \dots, n_y\}$ as the collection of all gridpoints where $(x, y) \in \mathcal{A}$ denotes the area $(x - 1, x] \times (y - 1, y]$. For our processed shoes, $n_x = 39$ and $n_y = 91$. The contact surface of a shoe refers to the region of the sole that typically interacts with the ground during wear, and is therefore responsible for generating footwear impressions.

In our analysis, we will follow [Spencer and Murray \(2020\)](#) and use dark pixel regions on the processed shoe print image as indicative of contact surface. We denote this contact surface as $C_s = (C_{s,a})_{a \in \mathcal{A}} \in [0, 1]^{\mathcal{A}}$ where, for instance, $C_{5,(19,45)} = 0.4$ tells us that the central pixel located at (19, 45)th coordinate of processed shoe print image of shoe 5 takes on the value 0.4 (indicating the presence of contact surface).

In addition to the C_s notation used for the shoe print image/contact surface, it will also be helpful to consider two related objects defined below:

- **Binary thresholded contact surface \tilde{C}_s :** Instead of considering continuous-valued contact surfaces, [Spencer and Murray \(2020\)](#) employed binary versions of the contact surface obtained by thresholding the pixels on the real-valued image. In this work, we use $\tilde{C}_s \in \{0, 1\}^{|\mathcal{A}|}$ to refer to a binarized version of the contact surface, defined according to

$$\tilde{C}_{s,a} = \begin{cases} 1 & \text{if } C_{s,a} > c_s \\ 0 & \text{otherwise,} \end{cases}$$

where the threshold $c_s > 0$ is chosen for each shoe s to accommodate subtle differences in background hue for each image. Figure 2b depicts the contact surface C_s and corresponding binary thresholded version \tilde{C}_s for shoe 2L (originally presented in Figure 1(c)).

- **Image gradient I_s :** The image gradient (sometimes referred to as the Sobel transformation) quantifies the rate at which the pixel intensity is changing in space at a given pixel in an image. Computed using the intensities of neighboring pixels, it tends to be useful for highlighting edges for feature extraction and object recognition. We apply the Sobel method via the EBImage ([Pau et al., 2010](#)) package to each processed contact surface C_s , yielding an image gradient object $I_s \in \mathbb{R}^{|\mathcal{A}|}$. An example of this object is depicted in Figure 2b; mathematical details appear in the supplement.

3.2. Configuration of Accidental Locations

Forensic investigators examine latent shoeprints found at crime scenes by focusing on unique damage patterns that develop through wear. These distinctive features—including scratches, holes, cuts, and perforations—are referred to as accidentals or randomly acquired characteristics ([Bodziak, 2017](#)). Unlike the original manufacturing design, these identifying marks accumulate as the shoe sole encounters various surfaces and debris during normal use. Forensic examiners detect accidentals on footwear by evaluating both the outsole itself and reference impressions, which are high-quality prints produced from the shoe under controlled laboratory conditions.

For each shoe print, the WVU database includes the locations of accidentals on the shoe outsole image, as determined by trained researchers. Figure 1(e) depicts raw accidental positions as points for the example shoes shown in Figures 1(a-d). Figure 2a depicts accidental

positions superimposed on an original and subsequent processed versions of a shoe print image.

To support our analysis, we summarized each WVU shoe's accidental locations by determining the total number of accidentals occurring in each coarsened grid coordinate. Note that this summary was performed after transforming the accidental coordinates into the processed space, thus accounting for coarsening and reflecting. We define the total accidental numbers in $a \in \mathcal{A}$ as a random variable $Y_{s,a}$ and the corresponding realizations of accidentals as $y_{s,a}$ for each shoe, i.e., $s \in \mathcal{S}$. So, we express the accidental information as a vector of counts $\mathbf{Y}_s := (Y_{s,a})_{a \in \mathcal{A}}$ and the corresponding realizations of accidentals are denoted by $\mathbf{y}_s := (y_{s,a})_{a \in \mathcal{A}}$.

4. Description of Model

4.1. General Formulation

Our primary goal is to develop and fit a tractable model for the distribution of a shoe's accidental configuration Y_s given its contact surface C_s . Recognizing that each Y_s can be viewed as a spatial point pattern observed over C_s , we approach this problem using tools from spatial statistics. Specifically, it is natural to frame each spatial configuration Y_s as a realization of spatial Poisson point process on C_s . Coarsening the resolution of the process to that of the C_s grid results in

$$Y_{s,a} | C_s \sim \text{Poisson}(\lambda_{s,a}) \text{ for all } s \in \mathcal{S} \text{ and } a \in \mathcal{A}.$$

Here, $\lambda_{s,a}$ denotes the intensity of the spatial Poisson process for shoe s at spatial coordinate a . Equivalently, $\lambda_{s,a}$ models the expected number of accidentals at position a on shoe s .

For each shoe s , we adopt a latent Gaussian model (Rue et al., 2017) for the log spatial intensity function $(\log(\lambda_{s,a}))_{a \in \mathcal{A}}$. Our model includes a spatially smoothed term to encourage correlations between neighboring grid points, and coefficients to incorporate the effect of various functions of C_s as covariates. Each shoe $s \in \mathcal{S}$ is also assigned its own intercept term as a random effect to capture how overall accidental counts vary broadly across shoes.

Rather than directly state our recommended model for $(\log(\lambda_{s,a}))_{a \in \mathcal{A}}$ in isolation, it is helpful to first establish a more general notation describing a class of models. This notation will make it easier to concisely formulate our model, as well as to compare it to possible variants, including those already proposed in the literature.

Consider the following general model for the log intensity:

$$(1) \quad \log(\lambda_{s,a}) := \beta_a^{\text{smooth}} + \beta_s^{\text{shoe}} + \sum_{\mathbf{i} \in \mathcal{I}} x_{s,a}^{\mathbf{i}} \beta_f^{\mathbf{i}} + \sum_{\mathbf{i} \in \mathcal{I}^*} x_{s,a}^{\mathbf{i}} \beta_{sv,a}^{\mathbf{i}}, \text{ where}$$

$$x_{s,a}^{\mathbf{i}} := (C_{s,a})^{i_1} (C_{s,a-h})^{i_2} (C_{s,a+h})^{i_3} (C_{s,a-v})^{i_4} (C_{s,a+v})^{i_5} (I_{s,a})^{i_6} \text{ for } \mathbf{i} \in \mathcal{I}$$

for some $\mathcal{I} \subseteq \{0, 1\}^6$ and $\mathcal{I}^* \subseteq \mathcal{I}$. Here,

- $(\beta_a^{\text{smooth}})_{a \in \mathcal{A}}$ denotes a spatially smoothed trend that is common to all shoes,
- $(\beta_s^{\text{shoe}})_{s \in \mathcal{S}}$ denotes the shoe-specific random intercepts,
- $(x_{s,a}^{\mathbf{i}})_{s \in \mathcal{S}, a \in \mathcal{A}, \mathbf{i} \in \mathcal{I}}$ denotes an interaction term involving the contact surface in the neighborhood of a and the image gradient at a ; $h = (1, 0)$, $v = (0, 1)$,
- $(\beta_f^{\mathbf{i}})_{\mathbf{i} \in \mathcal{I}}$ denotes fixed effect regression coefficients for interaction terms,
- $\beta_f^{\mathbf{0}}$ is the overall intercept term when $\mathbf{i} = (0, 0, 0, 0, 0, 0)$,
- $(\beta_{sv,a}^{\mathbf{i}})_{a \in \mathcal{A}, \mathbf{i} \in \mathcal{I}^*}$ denotes spatially varying regression coefficients for interaction terms.

Note that the choices of \mathcal{I} and \mathcal{I}^* control which contact surface interaction terms are excluded, which are considered as fixed effects, and which are considered as random effects. Note that $\mathcal{I}^* \subset \mathcal{I}$ is typically a proper subset for practical reasons; allowing all effects to vary in space would be both computationally and statistically intractable. Next, we will consider some concrete choices of \mathcal{I} and \mathcal{I}^* , representing our proposed model, some variants on it, and models that already exist in the literature. These models are summarized in Table 1.

4.2. Specific Models

Let us begin with the model we ultimately recommend, referred to as “Our Method” in Table 1. **Our method:** our recommended configuration is $\mathcal{I} = \{0, 1\}^6$, including fixed effect terms for all 64 interactions (up to order 6) involving the contact surface at a gridpoint, the image gradient at that gridpoint, and the contact surface at neighboring gridpoints. Furthermore, we suggest $\mathcal{I}^* = \{(1, 0, 0, 0, 0, 0), (0, 0, 0, 0, 0, 1), (1, 0, 0, 0, 0, 1)\}$, amounting to three spatially varying coefficients: one for the contact surface at a , one for the image gradient at a , and one for the interaction of these two terms. We demonstrate in Section 7 that this set-up exhibits superior predictive performance while maintaining a notion of interpretability. We hold off our discussion of the inference of its parameters until Section 5.

Existing methods: Next, it is helpful to consider contrasting these choices with existing contributions from the literature. To facilitate a direct comparison, we will focus on a subset of competitor models that can be framed using the general formulation outlined in Section 4.1; namely, we consider those approaches (Stone, 2006; Yekutieli et al., 2012; Spencer and Murray, 2020) that employ a Euclidean strategy for contact surface registration, and can be framed as latent Gaussian models. This ensures that the models can be tractably scaled up to the WVU database using the tools we describe in Section 5, thus facilitating a direct performance comparison in Section 7.

For competitors, let us first consider the simple uniform model of Stone (2006). It corresponds to a log intensity function that is uniform in space, equivalent to a prior on β_a^{smooth} that enforces equality for all $a \in \mathcal{A}$. The contact surface is not considered, corresponding to $\mathcal{I} = (0, 0, 0, 0, 0, 0)$, $\mathcal{I}^* = \emptyset$. Similarly, the spatial smoothing model of Yekutieli et al. (2012) is also independent of the contact surface with $\mathcal{I} = (0, 0, 0, 0, 0, 0)$, $\mathcal{I}^* = \emptyset$. However, β_a^{smooth} can vary smoothly with a in space. Spencer and Murray (2020) consider multiple variants on their model that exhibit similar performance; our comparison will focus on the “without scores and kernel” variant of their final model, as it is the most expressive of their models that can still be framed as a latent Gaussian model and thus tractably fit to the WVU database. All of their models incorporate the binary contact surface \tilde{C}_s in place of C_s , estimating a model equivalent to using $\mathcal{I} = (\{0, 1\}^5 \times \{0\})$. That is, all interactions of the contact surface are considered, but the image gradient is not. Finally, $\mathcal{I}^* = \emptyset$, as spatially varying coefficients are not considered.

Model Variants: Finally, to justify the specifics of our recommended configuration, it is worth considering additional variants on our model. We summarize four variants in Table 1. Unlike the work of Spencer and Murray (2020), they all use the continuous version of the contact surface.

- Variant A is configured according to $\mathcal{I} = (\{0, 1\}^5 \times \{0\})$ and $\mathcal{I}^* = \left\{ \mathbf{i} \in \mathcal{I} : \sum_{j=1}^5 \mathbf{i}_j \leq 2 \right\}$.
- Variants B, C, and D are configured according to $\mathcal{I} = \{0, 1\}^6$. For Variant B, $\mathcal{I}^* = \emptyset$. For Variant C, $\mathcal{I}^* = \{(1, 0, 0, 0, 0, 0)\}$. For Variant D, $\mathcal{I}^* = \{(1, 0, 0, 0, 0, 0), (0, 0, 0, 0, 0, 1)\}$.

Method	Intercept	Contact format	Contact		Contact Interactions Order					Image gradient (IG)	IG*Loc
			Loc	Nbd	2	3	4	5	6		
Our method / M(Final)	SV	Continuous	SV	F	F	F	F	F	F	SV	SV
M(variant A)	SV	Continuous	SV	SV	SV	F	F	F	F	x	x
M(variant B)	SV	Continuous	F	F	F	F	F	F	F	x	x
M(variant C)	SV	Continuous	SV	F	F	F	F	F	F	x	x
M(variant D)	SV	Continuous	SV	F	F	F	F	F	F	SV	x
M(b); Spencer and Murray (2020)	SV	Binary	F	F	F	F	F	F	x	x	x
M(a); Yekutieli et al. (2012)	SV	x	x	x	x	x	x	x	x	x	x
Uniform; Stone (2006)	F	x	x	x	x	x	x	x	x	x	x

TABLE 1

Description of different methods with fixed effects and spatially varying effects

Note: Loc: the pixel intensity, SV: spatially varying, F: fixed, x: not used in the model, *: interaction

5. Inference Procedure

Here, we present an inference procedure that is applicable to models formulated as in Section 4.1, including those in Table 1. For concreteness, our description will focus on the configuration of our proposed model. However, it is straightforward to adapt to other choices of \mathcal{I} and \mathcal{I}^* .

5.1. Bayesian Inference of Parameters

Recall the parameters from the model proposed in Section 4.1. Here, we reproduce them in vector form: $\beta^{\text{smooth}} \in \mathbb{R}^{|\mathcal{A}|}$, $\beta^{\text{shoe}} \in \mathbb{R}^{|\mathcal{S}|}$, $\beta_f \in \mathbb{R}^{|\mathcal{I}|}$, and $\beta_{sv}^i \in \mathbb{R}^{|\mathcal{A}|}$ for all $i \in \mathcal{I}^*$. For convenience, let us define a compact notation concatenating all of the vector parameters into a single vector $\theta \in \mathbb{R}^{|\mathcal{S}|+|\mathcal{I}|+(|\mathcal{I}^*|+1)|\mathcal{A}|}$:

$$(2) \quad \theta := \left(\beta^{\text{shoe}}, \beta_f, \beta^{\text{smooth}}, (\beta_{sv}^i)_{i \in \mathcal{I}^*} \right).$$

The likelihood can be written as:

$$(3) \quad \prod_{s=1}^{|\mathcal{S}|} \mathbb{P}(\mathbf{Y}_s = \mathbf{y}_s | C_s, \theta) = \prod_{s=1}^{|\mathcal{S}|} \prod_{a \in \mathcal{A}} \mathbb{P}(Y_{s,a} = y_{s,a} | C_s, \theta) = \prod_{s=1}^{|\mathcal{S}|} \prod_{a \in \mathcal{A}} \frac{e^{-\lambda_{s,a}} \lambda_{s,a}^{y_{s,a}}}{y_{s,a}!}.$$

Further, recall that our available data consist of accidental count-contact surface pairs $(Y_s, C_s) \in \mathbb{N}^{|\mathcal{A}|} \times [0, 1]^{|\mathcal{A}|}$ for each $s \in \mathcal{S}$, where $|\mathcal{S}| = 1300$. Our task is to use this available data for inference of the model parameters. For our purposes, we are most interested in estimating the parameters β^{smooth} , β_f , and β_{sv} . The shoe-specific intercept terms β^{shoe} are nuisance parameters, included to account for variability in total accidental counts across shoes.

Faced with many random effects and a desire to promote spatial smoothness, it is practical to approach this estimation problem from a Bayesian viewpoint. Specifically, by computing the posterior distribution of $\theta | (Y_s, C_s)_{s \in \mathcal{S}}$, we may derive estimates for the components of θ . To achieve this, we adopt the following hierarchical prior setup. We employ the following independent priors for each of $\beta_f, \beta^{\text{shoe}}, \beta_{sv}, \beta^{\text{smooth}}$.

For each $s \in \mathcal{S}$, we consider Gaussian priors on the shoe-specific intercepts as:

$$\beta_s^{\text{shoe}} | \tau_s \stackrel{\text{iid}}{\sim} \text{Normal} \left(0, \tau_s^{-1} \right) \text{ where, } \tau_s \sim \text{Exponential}(5 \times 10^{-5})$$

with $\text{Exponential}(\lambda)$ denoting an exponential distribution with rate parameter λ , and $\text{Normal}(\mu, \sigma^2)$ denoting a normal distribution with mean μ and variance σ^2 . Similarly, we assign independent Gaussian priors on each of the fixed effects:

$$\beta_f^i \stackrel{\text{iid}}{\sim} \text{Normal}(0, 1000) \text{ for each } i \in \mathcal{I}.$$

For our spatially varying parameters, we use constrained multivariate normal priors:

$$\beta^{\text{smooth}} \sim \text{Normal}(\mathbf{0}, \tau_{\text{sm}}^{-1} \mathbf{Q}^{-1}) \text{ with support } \{\beta^{\text{smooth}} \in \mathbb{R}^{|\mathcal{A}|} : \mathbf{1}^\top \beta^{\text{smooth}} = 0\},$$

$$\beta_{\text{sv}}^{\mathbf{i}} \sim \text{Normal}(\mathbf{0}, \tau_{\mathbf{i}}^{-1} \mathbf{Q}^{-1}) \text{ with support } \{\beta_{\text{sv}}^{\mathbf{i}} \in \mathbb{R}^{|\mathcal{A}|} : \mathbf{1}^\top \beta_{\text{sv}}^{\mathbf{i}} = 0\} \text{ for each } \mathbf{i} \in \mathcal{I}^*,$$

where $\mathbf{1} \in \mathbb{R}^{|\mathcal{A}|}$ is a vector consisting of ones. The precision matrix $\mathbf{Q} \in \mathbb{R}^{|\mathcal{A}| \times |\mathcal{A}|}$ is given by

$$\mathbf{Q}_{ij} = \begin{cases} n_k & \text{if } i = j = k, \\ -1 & \text{if } a_i \sim a_j, \text{ i.e. } \max(|a_{i1} - a_{j1}|, |a_{i2} - a_{j2}|) = 1, \\ 0 & \text{otherwise,} \end{cases}$$

where $a_i = (a_{i1}, a_{i2})$ denotes the (x, y) coordinates of the i th entry in \mathcal{A} , and $n_k = -\sum_{j \neq k} Q_{jk}$. This Besag dependence structure (Besag, 1974) promotes smoothing over the regular lattice of spatial coordinates; each gridpoint $a \in \mathcal{A}$'s neighborhood is defined as those gridpoints $a' \in \mathcal{A}$ that share at least a boundary point (i.e. queen adjacency). This neighborhood graph structure is depicted in the left panel of Figure 3.

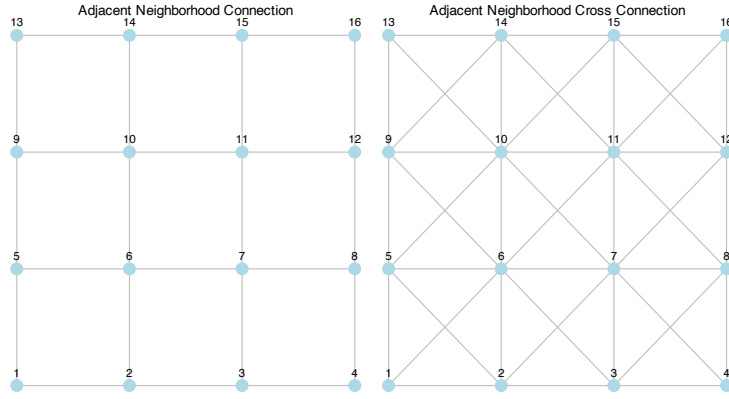


Fig 3: Adjacent neighborhood connections if the number of nodes were 16. The left panel neighborhood connection does not involve the diagonal connection. The right panel considers the diagonal connection. We have considered the neighborhood structure as mentioned in the right panel for all the nodes in the grid $[30, 68] \times [5, 95]$.

Note that the precision matrix \mathbf{Q} corresponds to the graph Laplacian for this adjacency structure, implying that it is doubly-centered and therefore not full-rank. To compensate, we included the sum-to-zero constraints on the vectors of coefficients. This support restriction is a common convention (Keefe, Ferreira and Franck, 2018) to ensure the prior is proper.

The τ_{sm} and $(\tau_{\mathbf{i}})_{\mathbf{i} \in \mathcal{I}}$ hyperparameters control the level of prior spatial smoothing over β^{smooth} and β_{sv} , respectively. For these, we employ independent hyperpriors:

$$\tau_{\text{sm}} \sim \text{Exponential}(5 \times 10^{-4}),$$

$$\tau_{\mathbf{i}} \sim \text{Exponential}(5 \times 10^{-4}) \text{ for all } \mathbf{i} \in \mathcal{I}^*.$$

Note that if \mathcal{I}^* is large, it may be computationally impractical to independently infer $\tau_{\mathbf{i}}$ for all \mathbf{i} . In these cases, we limit hyperparameter inference to those $\tau_{\mathbf{i}}$ corresponding to main effects (i.e. $\mathbf{i}^\top \mathbf{i} = 1$). For higher order interactions, we consider the fixed value of $\tau_{\mathbf{i}} = 100$. However, for notational succinctness, we consider priors on all elements of \mathcal{I}^* in our expressions below.

All together, we have parameters θ whose prior distribution is governed by hyperparameters $\psi = (\tau_s, \tau_{\text{sm}}, \tau_{\mathbf{i}}; \mathbf{i} \in \mathcal{I}^*)$. Note that, conditional on the hyperparameters ψ , our joint prior

on θ is a constrained multivariate Gaussian. Specifically, our full prior takes the form $\pi_0(\theta, \psi) = \pi_0(\theta | \psi)\pi_0(\psi)$ for

$$(4) \quad \pi_0(\psi) := \left(\tau_s \tau_{sm} \prod_{\mathbf{i} \in \mathcal{I}^*} \tau_{\mathbf{i}} \right) e^{-5000(10\tau_s + \tau_{sm} + \sum_{\mathbf{i} \in \mathcal{I}^*} \tau_{\mathbf{i}})},$$

$$\pi_0(\theta | \psi) := \sqrt{\frac{|\Sigma(\psi)|_*}{(2\pi)^d}} \exp\left(-\frac{\theta^\top \Sigma(\psi) \theta}{2}\right), \text{ for}$$

$$(5) \quad d := |\mathcal{S}| + |\mathcal{I}| + (|\mathcal{I}^*| + 1)(|\mathcal{A}| - 1), \text{ and}$$

$$(6) \quad \Sigma(\psi) := (\tau_s \mathbb{I}_{|\mathcal{S}|}) \oplus (1000 \mathbb{I}_{|\mathcal{I}|}) \oplus (\tau_{sm} \mathbf{Q}) \bigoplus_{\mathbf{i} \in \mathcal{I}^*} \tau_{\mathbf{i}} \mathbf{Q},$$

where \mathbb{I}_n denotes the $n \times n$ identity matrix, \oplus denotes block diagonal concatenation, and the support of $\pi_0(\theta | \psi)$ is restricted to $\theta \in \{\mathbb{R}^{d+1+|\mathcal{I}^*|} : \mathbf{1}^\top \beta^{\text{smooth}} = 0, \mathbf{1}^\top \beta_{sv}^{\mathbf{i}} = 0 \text{ for all } \mathbf{i} \in \mathcal{I}^*\}$, and $|\Sigma|_*$ denotes the generalized determinant of Σ —the product of the d nonzero eigenvalues.

Combining the prior and likelihood, our target posterior thus takes the form:

$$(7) \quad \pi(\theta, \psi | \{\mathbf{Y}_s = \mathbf{y}_s\}_{s=1}^S, \{C_s\}_{s=1}^S) \propto \prod_{s=1}^S \prod_{a \in \mathcal{A}} \frac{e^{-\lambda_{s,a} \lambda_{s,a}^{y_{s,a}}}}{y_{s,a}!} \sqrt{\frac{|\Sigma(\psi)|_*}{(2\pi)^d}} \exp\left(-\frac{\theta^\top \Sigma(\psi) \theta}{2}\right) \pi_0(\psi),$$

where $\pi_0(\psi)$ is given as in (4), d is given as in (5), $\Sigma(\psi)$ is given as in (6), and the support is restricted according to the sum-to-zero constraints described above. Recognizing that this set-up does not yield a closed form solution for the normalization constant, we instead derive a computationally tractable approximate inference strategy for θ .

5.2. Inference Strategy

For our suggested model M(Final) in Table 1, the full posterior distribution described by (15) involves $d + 1 + |\mathcal{I}^*| = 14261$ parameters, as well as four hyperparameters. Our available data consists of counts and covariate values for a relatively large number, $|\mathcal{S}| \times |\mathcal{A}| = 1300 \times 3549 \approx 4.6 \times 10^6$, of individual gridpoints. Consequently, reliable inference of θ via Markov chain Monte Carlo is not computationally feasible within a reasonable time frame given our available resources. Instead, we have formulated our model such that the posterior in (15) adheres to a specific structure—that of a latent Gaussian model (LGM). LGMs admit a fast computation via a technique known as integrated nested Laplace approximations or INLA (Rue, Martino and Chopin, 2009).

5.2.1. Review of Latent Gaussian Models and INLA

LGMs: Latent Gaussian Models (LGMs) are a broad class of hierarchical statistical models in which the observed data $\mathbf{y} = (y_1, \dots, y_m)^\top$ are assumed to be conditionally independent given a Gaussian random field \mathbf{x} and hyperparameters ψ . Specifically, $\mathbf{x} | \psi \sim \text{Normal}(\mathbf{0}, \mathbf{Q}(\psi_1)^{-1})$, where the precision matrix $\mathbf{Q}(\psi_1)$ depends on hyperparameters ψ_1 , and each y_i is independently distributed according to a distribution $p(y_i | \eta_i(\mathbf{x}), \psi_2)$ with additional hyperparameters ψ_2 such that $\psi = (\psi_1, \psi_2)$. Here, each $\eta_i(\cdot)$ denotes an observation-specific function of the latent field \mathbf{x} .

Models following this set-up can thus be expressed as:

$$\psi \sim p(\psi), \text{ where } \psi := (\psi_1, \psi_2);$$

$$\mathbf{x} | \psi_1 \sim \text{Normal}(\mathbf{0}, \mathbf{Q}(\psi_1)^{-1});$$

$$p(\mathbf{y} | \mathbf{x}, \psi_2) = \prod_{i=1}^m p(y_i | \eta_i(\mathbf{x}), \psi_2).$$

The prior distribution $p(\psi)$ is typically specified independently of \mathbf{x} . The resulting joint distribution therefore factorizes as $p(\mathbf{y}, \mathbf{x}, \psi) = p(\psi) p(\mathbf{x} | \psi_1) \prod_{i=1}^m p(y_i | \eta_i(\mathbf{x}), \psi_2)$.

Typically, the functions $\eta_i(\mathbf{x}) = \mathbf{b}_i^\top \mathbf{x}$ are observation-specific linear combinations of the latent field; observed covariates can then be incorporated in the weight vector \mathbf{b}_i . Popular models adhering to this framework include logistic regression models with random effects (Rue, Martino and Chopin (2009)), spatio-temporal models (Simpson et al. (2016)), and survival models (Martino, Akerkar and Rue (2011)). Posterior that factorize this way are amenable to fast and accurate approximation via INLA.

INLA: Bayesian inference for LGMs typically targets entries of \mathbf{x} and ψ , with \mathbf{x} being of primary interest. Recognizing that the joint posterior $p(\psi, \mathbf{x} | \mathbf{y})$ is rarely available in closed form, practitioners typically approximate $p(\psi, \mathbf{x} | \mathbf{y})$ using tools like Markov chain Monte Carlo (MCMC). However, reliable MCMC is often computationally infeasible when \mathbf{x} is high-dimensional, or the number of data points m is relatively large.

Instead, INLA (Rue, Martino and Chopin (2009)) is a fast alternative for doing inference under LGMs, producing reliable approximations of the individual marginal posteriors $p(\mathbf{x}_j | \mathbf{y})$ for each entry j in the Gaussian latent field \mathbf{x} . This is accomplished by leveraging the Gaussianity of the latent field to implement accurate Laplace approximations to $p(\psi | \mathbf{y})$ and to $p(\mathbf{x}_j | \mathbf{y}, \psi)$, followed by numerical integration over ψ .

The resultant marginal posterior approximations $\tilde{p}(\mathbf{x}_j | \mathbf{y})$ for each j provide an avenue to estimate \mathbf{x}_j via $\hat{\mathbf{x}}_j$, the approximate posterior mean. Combined, the result is $\hat{\mathbf{x}}$, a natural point estimator of \mathbf{x} . Posterior credible intervals or marginal standard deviations can be used to quantify univariate uncertainty.

It is worth noting that INLA provides primarily accurate approximations to marginal posterior distributions and related low-dimensional summaries; the full joint posterior of \mathbf{x} is not available in closed form. Nonetheless, univariate and low-dimensional summaries are typically the primary inferential targets in applications. Additional details on the specifics of INLA (Rue, Martino and Chopin (2009), Rue et al. (2017)) are available in the supplement. A fast implementation of INLA is available within the RINLA package in R (Rue et al. (2024)).

5.2.2. Framing Our Approach as a LGM

The posterior of our model, described in (15) with λ defined as in (10), satisfies the criteria of a LGM, and is thus amenable to fast marginal inference via INLA. Specifically, the latent Gaussian field is given by $\mathbf{x} = \boldsymbol{\theta}$ as in (2), the hyperparameters $\psi = (\tau_s, \tau_{\text{sm}}, \tau_i; i \in \mathcal{I}^*)$ as in Section 5.1. The response \mathbf{y} is given by $(Y_{s,a})_{s \in \mathcal{S}, a \in \mathcal{A}}$, with entries given by accidental counts in each contact surface gridpoint on each shoe. Indexing according to s and a , we thus have:

$$\eta_{s,a}(\boldsymbol{\theta}) = \beta_a^{\text{smooth}} + \beta_s^{\text{shoe}} + \sum_{i \in \mathcal{I}} x_{s,a}^i \beta_f^i + \sum_{i \in \mathcal{I}^*} x_{s,a}^i \beta_{sv,a}^i.$$

Note that this expression is linear in $\boldsymbol{\theta}$ in that it can be expressed as $\mathbf{b}_i^\top \boldsymbol{\theta}$ for some $\mathbf{b}_i \in \mathbb{R}^{d+1+|\mathcal{I}^*|}$.

Because our model is posed as a relatively standard application of a 2-dimensional spatial LGM, inference is straightforward to carry out using the tools available in the RINLA package. We rely on RINLA for the relevant computations in Section 6 and Section 7. Note that the sum-to-zero constraint on the spatially varying effects is standard in RINLA.

In the next section, we inspect posterior mean estimates of the model parameters derived from the INLA marginal posteriors, focusing on the inferred spatial structure and the spatially varying covariate effects.

6. Model fit

Using RINLA to fit our proposed model to the full dataset yields posterior point estimates for our main parameters of interest; namely, the spatially varying coefficients β^{smooth} and $(\beta_{\text{sv}}^i)_{i \in \mathcal{I}^*}$, and the fixed coefficients $(\beta_f^i)_{i \in \mathcal{I}}$. These specific fitted values describe accidental propensity varies across space, local contact surface intensity, and their interactions. In this section, we explore and interpret our fitted values for these parameters. Because they are straightforward to visualize as a two-dimensional grid, we begin with the spatially varying effects.

6.1. Spatial Effects

For the four spatially varying effects, we consider both their raw estimated values (Figure 4) and their effect in the context of a specific shoe (Figure 5).

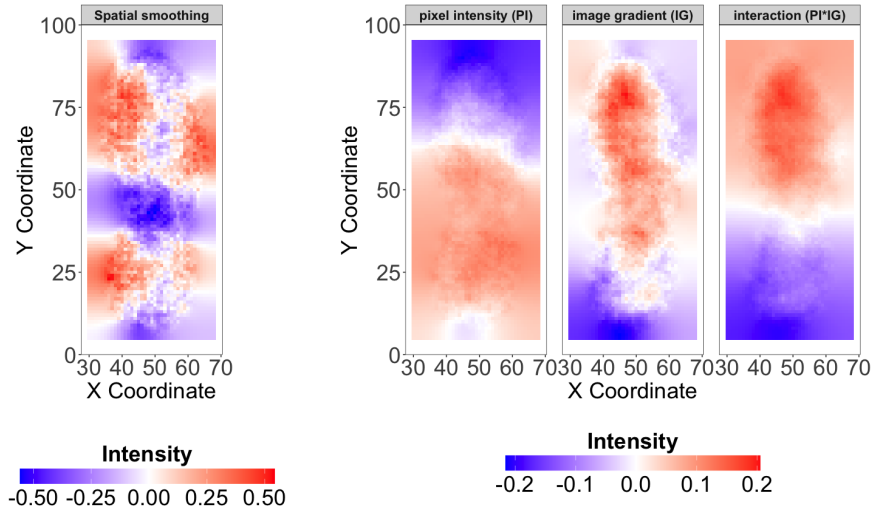


Fig 4: Overall spatial smoothing (β^{smooth}) and three raw spatially varying coefficients of pixel intensity, image gradient, and their interaction. The red patches demonstrate high intensity, and the blue patches lower intensity across coefficient values.

The left panel of Figure 4 shows a heatmap of the posterior mean of the spatially varying intercept β^{smooth} . Our inference strategy constrains the sum of β^{smooth} to 0, so red regions indicate above typical accidental propensity, whereas blue regions depict lower. We observe that the center portion around $[40, 60] \times [30, 55]$ has relatively low intensity compared to its surrounding area. This suggests that, even controlling for contact surface, accidentals are less likely to occur at the arch of the shoe. Likewise, the tip of the toe and tip of the heel also exhibit lower accidental propensity. In contrast, the outsole below the sides of the toebox have relatively high propensity for accidentals, as does the inner heel. Note that the range of this effect is approximately 1, meaning the highest propensity regions are prone to roughly $e^1 \approx 2.7$ as many accidentals as low propensity regions of lowest propensity.

Next, we consider the right panel of Figure 4, depicting three spatially varying coefficients:

$\beta_{\text{sv}}^{\mathbf{i}_1}$ with $\mathbf{i}_1 = (1, 0, 0, 0, 0, 0)$ (spatially varying effect of pixel intensity),

$\beta_{\text{sv}}^{\mathbf{i}_2}$ with $\mathbf{i}_2 = (0, 0, 0, 0, 0, 1)$ (spatially varying effect of image gradient), and

$\beta_{sv}^{i_3}$ with $\mathbf{i}_3 = (1, 0, 0, 0, 0, 1)$ (spatially varying effect of their interaction).

Recall from Section 5 that the sum of each of these coefficients is constrained to 0, with red indicating an above typical covariate effect, and blue being below typical. Care must be taken in interpretation: the presence of corresponding fixed effects in the model means that negative values of the spatially varying coefficient does not necessarily imply the covariate has a negative effect. The effect is negative only if the sum of both the fixed and spatially varying effects is negative.

Because these three spatially varying coefficients impact accidental propensities through the contact surface covariate, it is challenging to interpret them in isolation. For instance, though shown as strong, the effects shown along the rectangular boundary are unlikely to be impactful in practice because they rarely correspond to nonzero contact surface. Instead, it is helpful to consider the effects in the context of a given shoe as in Figure 5.

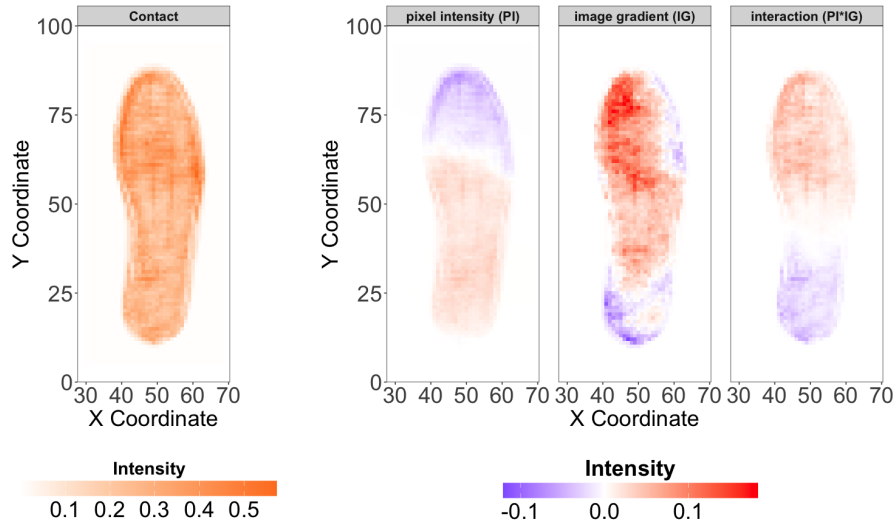


Fig 5: Contact and spatially varying coefficients multiplied with the covariates of an example shoe 202-L. The red patches demonstrate high intensity, and the blue patches lower intensity across coefficient values.

Figure 5 depicts the product of the spatially varying coefficients with their corresponding covariates for an example shoe s' (corresponding to 202-L in the WVU database). Namely, Figure 5 shows how $x_{s',a}^i \beta_{sv}^i$ varies across $a \in \mathcal{A}$ for $\mathbf{i} = \mathbf{i}_1, \mathbf{i}_2$, and \mathbf{i}_3 .

With this additional visual aid, we can better see that coefficient for pixel intensity (\mathbf{i}_1) varies smoothly across the shoe surface, with larger effects in the lower and central regions and smaller effects toward the upper forefoot. In contrast, the image gradient coefficient shows stronger spatial heterogeneity, with stronger positive effects at the inner toe, and relatively weaker effects at the heel and outer toe. This suggests that edge-related features contribute differently depending on location. The interaction term exhibits a comparatively smoother structure, with stronger effects concentrated in the forefoot and weaker effects toward the heel.

6.2. Contact Surface Effects

Next, we consider our estimates of the fixed effects $(\beta_f^i)_{i \in \mathcal{I}}$ modeling the effect of the contact surface on accidental propensities. It is challenging to interpret each effect on its own, as their

effects are intertwined through the full set of interactions. Instead, we consider the cumulative fixed effect ($\sum_{i \in \mathcal{I}} x_{s,a}^i \beta_f^i$) below. In Figure 6, we present the contact surface (left panel) and the corresponding cumulative fixed effect (right panel) for two example shoes, 287-R and 543-R. In the right panel, the warmer the color, the higher the contribution to the accidental propensities.

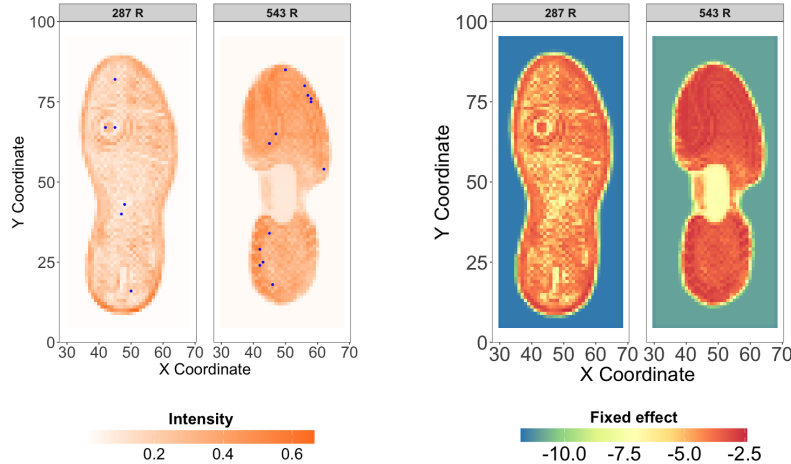


Fig 6: Contact surface and the corresponding cumulative fixed effects ($\sum_{i \in \mathcal{I}} x_{s,a}^i \beta_f^i$) over different spatial locations for shoe 287-R and 543-R.

Note that shoe 543-R has a high mid arch, resulting in low contact surface intensity and lower accidental propensity in the arch region. Similarly, there is a circular pattern of lower intensity contact surface on shoe 297-R, translating to lower accidental propensity. In contrast, the inner heel of shoe 543-R is a region of especially high intensity and uniform contact surface, corresponding to especially high accidental propensity. A similar effect is shown at the tip of the heel of 287-R. Finally, for each shoe, the perimeter of low-intensity contact surface neighboring the shoe nonetheless corresponds to moderate accidental propensity, implying that the high-intensity neighboring pixels are driving up the propensity.

Overall, the most strikingly apparent observation from comparing the panels in Figure 6 is that pixels with more contact surface tend to have higher accidental propensity. To further validate this conclusion, Figure 7 plots the exponentiated cumulative fixed effect $\exp(\sum_{i \in \mathcal{I}} x_{s,a}^i \beta_f^i)$ for Shoe 287-R against two main covariates: the pixel-wise contact surface $x_{s,a}^i = C_{s,a}$ and the image gradient $x_{s,a}^{i_2} = \mathcal{I}_{s,a}$.

The left panel of Figure 7 shows a decisive marginal relationship between the two variables, indicating that pixel-wise contact surface value is a dominant driver of the fixed effect component, while the impact of the image gradient is relatively weaker. Note that neighboring pixel intensities tend to be strongly correlated, which can make it difficult to isolate individual effects. Nevertheless, the additional noise around the main trend in the left panel captures the impact of the neighboring contact intensities and the image gradient.

For additional exploration of this relationship, Figure 8 displays the neighboring pixel intensities for the ten highest- and ten lowest-ranking coordinates a on shoe 287-R, ranked according to the cumulative fixed effect $\sum_{i \in \mathcal{I}} x_{s,a}^i \beta_f^i$, where only pixels with intensity greater than 0.2 are included to exclude regions outside the shoe print. The highest-ranking coordinates exhibit pronounced pixel intensity concentrated in the central region (average intensity .4), indicating stronger and more coherent surface contact. In contrast, the lowest-ranking

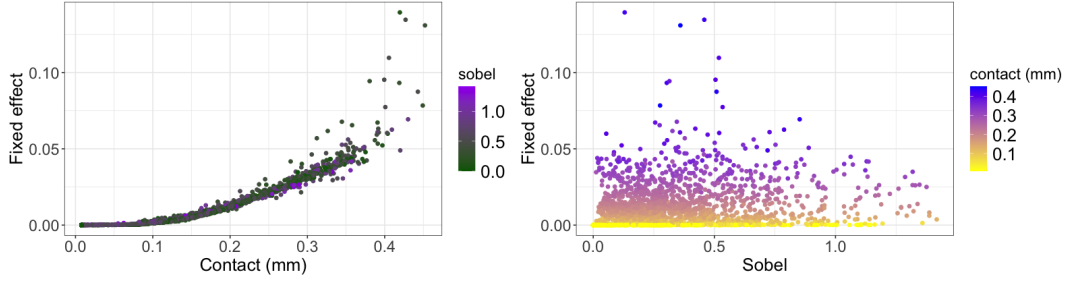


Fig 7: Contact surface and sobel/image gradient vs exponentiated cumulative fixed effect ($\exp(\sum_{i \in I} x_{s,a}^i \beta_f^i)$) for Shoe 287-R. Contact surface intensity has a major contribution, whereas Sobel has a less significant contribution to the cumulative fixed effect.

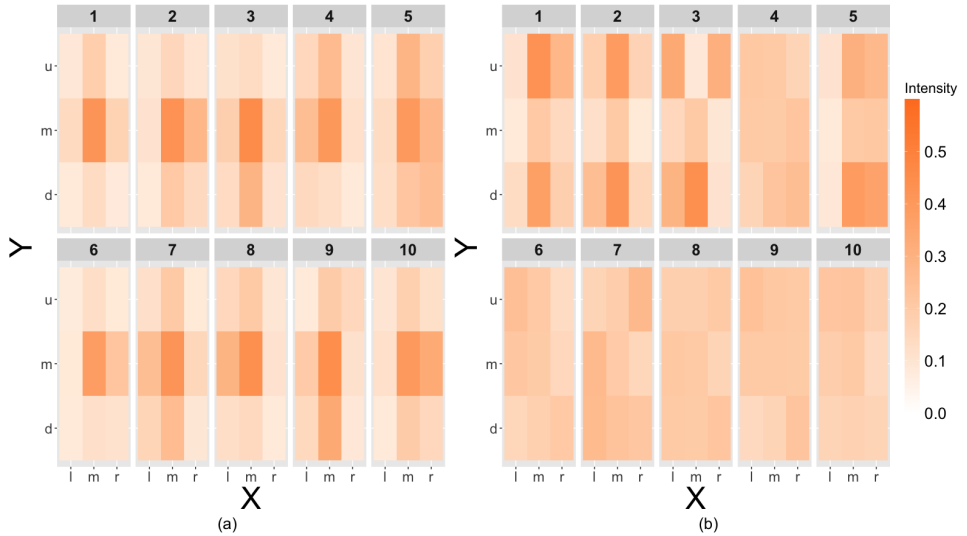


Fig 8: Top 10 (left) combinations and bottom 10 (right) combinations ranked by the fixed effect ($(\sum_{i \in I} x_{s,a}^i \beta_f^i)$) of a test shoe 287-R. The lower combinations show the flatter pattern in pixel shoe surfaces. The top combinations have higher pixel intensity in the middle.

coordinates display flatter and more diffuse intensity (average intensity 0.15) patterns, consistent with worn or low-contact areas of the shoe. Overall, higher pixel intensity is systematically associated with larger values of $\sum_{i \in I} x_{s,a}^i \beta_f^i$, whereas regions with reduced or uneven contact contribute less to the cumulative fixed effect. These results provide visual confirmation that increased contact surface is strongly associated with the magnitude of the cumulative fixed effect.

6.3. Predictive Distribution

Recall from Section 2.1 that, for a given shoe s , the distribution of its accidental configuration \mathbf{Y}_s conditional on its contact surface C_s plays a central role in evaluating accidental-based random match probabilities. Thus far, we have interpreted components of the fitted model by examining the cumulative fixed effects $\sum_{i \in I} x_{s,a}^i \beta_f^i$ separately from the spatially varying effects. We now combine these components to obtain the predictive distribution of accidental locations,

$\mathbf{Y}_s \mid C_s$. Accurately characterizing this predictive distribution is our primary objective, as it is the object used to compute random match probabilities.

As shown in Section 4.1, our model defines a spatial Poisson process (Kingman, 1993) over the discretized shoe domain \mathcal{A} . Consequently, conditional on C_s and the model parameters θ , the accidental locations for shoe s may be viewed as independent draws from \mathcal{A} , with probability mass proportional to the intensity $\lambda_{s,a}$. The resulting predictive spatial distribution is therefore characterized by

$$q(C_s, \theta) := (q_a(C_s, \theta))_{a \in \mathcal{A}},$$

where the probability $q_a(C_s, \theta)$ is defined as:

$$\begin{aligned} q_a(C_s, \theta) &:= \frac{\lambda_{s,a}}{\sum_{a' \in \mathcal{A}} \lambda_{s,a'}} \\ (8) \quad &= \frac{\exp\left(\sum_{\mathbf{i} \in \mathcal{I}} x_{s,a}^{\mathbf{i}} \beta_f^{\mathbf{i}} + \sum_{\mathbf{i} \in \mathcal{I}^*} x_{s,a}^{\mathbf{i}} \beta_{sv,a}^{\mathbf{i}} + \beta_a^{\text{smooth}}\right)}{\sum_{a' \in \mathcal{A}} \exp\left(\sum_{\mathbf{i} \in \mathcal{I}} x_{s,a'}^{\mathbf{i}} \beta_f^{\mathbf{i}} + \sum_{\mathbf{i} \in \mathcal{I}^*} x_{s,a'}^{\mathbf{i}} \beta_{sv,a'}^{\mathbf{i}} + \beta_{a'}^{\text{smooth}}\right)}. \end{aligned}$$

Importantly, this distribution is independent of the shoe-specific random effect β_s^{shoe} , since the multiplicative factor $\exp(\beta_s^{\text{shoe}})$ cancels in the normalization. Thus, the predictive spatial distribution of an arbitrary accidental on shoe s is fully determined by its contact surface C_s and the global model parameters θ through $q(C_s, \theta)$.

Figure 9 illustrates the contact surface C_s , the associated image gradient I_s , and the resulting predictive distribution $q(C_s, \theta)$ for two example shoes from the WVU database. The displayed predictive distributions are computed using posterior mean estimates of θ obtained by fitting our final model with the inference strategy described in Section 5.

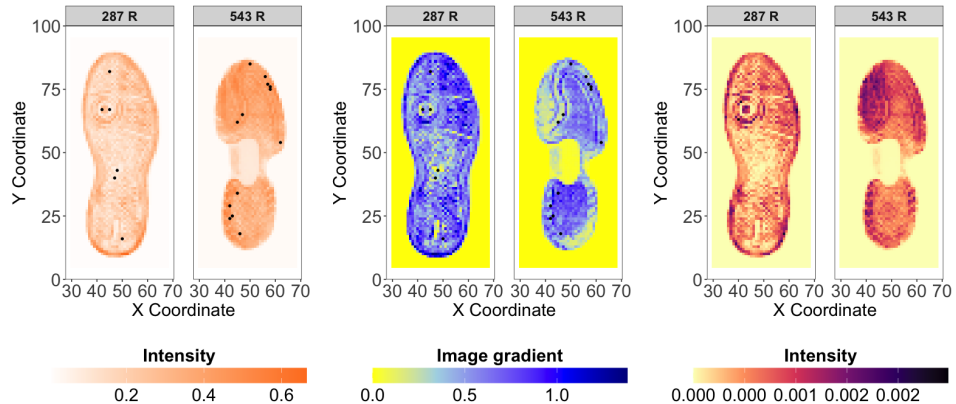


Fig 9: Contact, image gradient, and posterior predictive distribution plots for two different shoeprints 287-R and 543-R. In the third panel, the darker color demonstrates the higher intensity of the posterior probability over the contact surface.

In the Figure 9, the predictive intensity (third panel) is inhomogeneous across the shoe surface, ranging from 0 to .002, which implies the absolute difference for higher probability regions is approximately .002 higher than the low probability regions. These are largely driven by the contact surface (C_s) and image gradient, and the parameters estimated from the model M(Final). For example, within the logo (287-R), the pixel intensity and image gradient are higher, resulting in higher contrast with the surrounding area ($X = 45, Y = 67$). We also

observe that two exact accidentals appear in the region. In contrast, low image gradient and pixel intensity result in lower predictive intensity. For example, in the middle of the shoe 543-R (around $(X = 50, Y = 50)$), the contact surface intensity and image gradient are close to 0, resulting in the probability close to 0. In the original image of 543 R, we do not observe any accidentals around that region. Thus, if a shoe print is provided, the above model can capture the probability of the accidental occurrence just based on the contact surface, the derived image gradient intensity, and the coefficients estimated from the fitted model $M(\text{Final})$.

Although visual inspection of individual predictive distributions can provide insight into qualitative aspects of the fitted model, our primary motivation for estimating these distributions is to compute accidental-based random match probabilities. Consequently, the most meaningful assessment of our estimate of $q(C_s, \theta)$ is its predictive performance. Section 7 is devoted to this evaluation. Before turning to that assessment, however, we compare the findings presented here with those of related models in the existing literature.

6.4. Comparison to Existing Literature

Some of the insights presented above are consistent with existing findings in the literature, while others appear to be new.

Beginning with β^{smooth} , the left panel of Figure 4 shares several similarities with [Richetelli and Speir \(2022\)](#), which depicts a summary of the aggregated spatial distribution of total accidental counts across the WVU database after polar-coordinate registration. In particular, they also show higher accidental propensity below the inner side of the toebox, at the inner heel, and (to a lesser extent) along the outer side of the toebox. Likewise, both figures show fewer accidentals occurring at the arch of the shoe, as well as near the toe tip and heel tip.

However, the two figures also exhibit key differences. Notably, [Richetelli and Speir \(2022\)](#) shows a dip in accidental counts near the perimeter of the shoe, as well as substantial spatial variation across bins; some coordinates have more than an order-of-magnitude difference in accidental counts relative to others. In contrast, our Figure 4 shows no comparable drop along the perimeter, and the overall range of spatial effects is much smaller, with the highest-propensity regions exhibiting roughly $e^1 \approx 2.7$ times the intensity of the lowest-propensity regions. This reduced variation can be largely attributed to the fact that our model explicitly controls for contact surface. Similarly, the difference along the perimeter can be explained by differences in registration, as the polar-coordinate approach enforces a direct perimeter-to-perimeter correspondence, whereas our Euclidean registration does not.

Another relevant comparison for β^{smooth} is provided by [Spencer and Murray \(2020\)](#), Supplemental Figure 1), which depicts how the fitted spatial effect varies bin-to-bin under a model that also uses Euclidean registration and fixed effects to control for the contact surface. That model, however, is applied to a different dataset (JESA). The resulting spatial surface shares limited similarities with Figure 4; both exhibit increased accidental propensity at the inner heel, and both display a similar overall magnitude of spatial variation (on the order of a factor of two). This level of variation is substantially lower than that observed in models that do not control for contact surface (e.g., Figure 2 of [Damary et al., 2019](#)), emphasizing the importance of accounting for contact surface when computing random match probabilities.

Turning to the remaining spatially varying effects, there is no existing baseline against which to compare $\beta_{\text{sv}}^{i_1}$, $\beta_{\text{sv}}^{i_2}$, and $\beta_{\text{sv}}^{i_3}$, as our model is the first to incorporate spatially varying effects for the contact surface-related covariates. Nonetheless, our finding that accounting for such effects improves model performance. This result, as well as the specific spatial variation we observe, may be of independent interest to shoe examiners.

Finally, for the fixed effects associated with the contact surface, the closest comparison in the literature is that of [Spencer and Murray \(2020\)](#). While their model employs a binary

representation of the contact surface and ours uses a continuous one, the substantive conclusions are largely consistent. In both models, grid points containing, or neighboring, more contact surface tend to exhibit higher accidental propensity, whereas those neighboring little or no contact surface tend to exhibit lower accidental propensity. Moreover, incorporation of the contact surface appears to be a primary driver of improved model performance in both settings.

7. Model Evaluation and Comparison

Recall that the primary use case for our model is the estimation of reliable random match probabilities. Accordingly, our goal is to accurately quantify the relative frequency with which different spatial patterns of accidentals arise on shoe soles, conditional on the contact surface. Specifically, we seek to model $P(Y_s = y_s | C_s)$ in a way that is practically reliable for the accidentals y_s and contact surfaces C_s encountered in forensic casework. Reliable estimation of this quantity is important for assessing the likelihood of a coincidental match between accidentals observed on a shoe and those present in a crime scene impression. Conversely, unreliable estimates may lead to systematic over or under-estimation of random match probabilities, thereby risking misleading evidentiary conclusions in courtroom settings.

It is thus appropriate to evaluate model performance by assessing how reliably $P(Y_s = y_s | C_s)$ is estimated for shoes in the WVU dataset (see section 3). To avoid optimistic bias arising from evaluating the model on the same data used for fitting, we adopt a data-splitting strategy. Specifically, we use 10-fold cross-validation, in which the dataset is randomly partitioned into ten equally sized subsets of shoes; in each fold, nine subsets are used for model fitting and the remaining subset is held out for evaluation.

For each held-out shoe in the validation set, the probability $P(Y_s = y_s | C_s)$ can be decomposed as a product of two components:

1. a multinomial probability mass function evaluation to quantify the probability of the observed spatial configuration y_s , and
2. a Poisson probability mass function evaluation to quantify the probability of observing the total number of accidentals in y_s .

Details of this decomposition are provided in Section 1.2 and 1.3 of the Supplement.

Recall that, in typical forensic settings, only a subset of accidentals present on the source shoe are detectable in a crime scene impression. As a result, the total number of accidentals—captured by the Poisson component of $P(Y_s = y_s | C_s)$ —is generally not of primary relevance for computing random match probabilities. Instead, the spatial distribution of accidentals, as characterized by the multinomial component, is used to derive our metric for model evaluation.

Specifically, we employ the following per-shoe evaluation metric:

$$(9) \quad m(Y_s = y_s | C_s, \theta) = \frac{\sum_{a \in \mathcal{A}} y_{s,a} \log(q_a(C_s, \theta))}{\sum_{a \in \mathcal{A}} y_{s,a}} - \log(\delta_{\mathcal{A}}),$$

where $q_a(C_s, \theta)$ is defined as in (8), and $\delta_{\mathcal{A}} = \frac{783 \times 336}{91 \times 39} \approx 74.13$.

The quantity in (9) corresponds to the natural logarithm of the multinomial component of $P(Y_s = y_s | C_s)$, subject to three modifications. First, the expression is normalized by the total number of accidentals on the shoe, allowing comparisons across shoes with differing accidental counts. Second, the multinomial coefficient is omitted for the same reason. Finally, the constant $\delta_{\mathcal{A}}$ is included to account for the coarseness of the grid \mathcal{A} .

In the case of the WVU database, the original images of the laboratory generated shoe impressions were provided at a resolution of 869×869 , corresponding to a 783×336 region containing the outsole impressions. The adjustment by $\delta_{\mathcal{A}}$ therefore corresponds to converting probabilities defined on the coarsened grid back to the original resolution, implicitly distributing

probability mass uniformly across the pixels comprising each grid cell. While we do not explore alternative coarsening schemes in this work, we highlight this adjustment to emphasize a subtle challenge that arises when comparing results across different databases, discretization levels, and registration strategies.

Rather than evaluate our proposed model in isolation, we provide context by comparing our model’s data-splitting performance to related models discussed in Section 2.3, all expressed within our latent Gaussian model framework as described in Section 4.2. A summary of these models is available in Table 1. Specifically, we collected the metric in (9) for all 1300 WVU database shoes for our model M(Final) along with four competing models from Table 1: the Uniform model as in Stone (2006); M(a), a spatially model without contact surface effects as in Yekutieli et al. (2012); M(b), a binary contact surface model as in Spencer and Murray (2020); M(Variant A), a variant of our model with 15 spatially varying coefficients for the contact surface, but no image gradient terms.

A summary of this comparison is provided in Table 2, which reports the average value of the metric in (9) across the 130 held-out shoes in each fold. The relative performance of the five models is consistent across folds. Our method achieves the best performance in every fold, followed closely by the M(Variant A) specification of our model. The next best-performing approach is M(b) from Spencer and Murray (2020), after which there is a substantial drop in performance among models that do not incorporate contact surface information. This pattern reinforces the importance of accounting for the contact surface when computing reliable random match probabilities.

Fold	Uniform	Intercept SV M(a)	Binary contact M(b)	15 SV M(variant A)	Our Method/ M(Final)
1	-12.480	-11.920	-11.451	-11.344	-11.311
2	-12.480	-11.940	-11.463	-11.336	-11.314
3	-12.480	-11.921	-11.460	-11.362	-11.334
4	-12.480	-11.887	-11.475	-11.327	-11.297
5	-12.480	-11.900	-11.459	-11.348	-11.326
6	-12.480	-11.944	-11.545	-11.452	-11.426
7	-12.480	-11.882	-11.521	-11.388	-11.359
8	-12.480	-11.904	-11.402	-11.331	-11.287
9	-12.480	-11.884	-11.466	-11.353	-11.328
10	-12.480	-11.913	-11.500	-11.395	-11.364

TABLE 2

Average model performance as measured by (9) across ten folds. Top performer for each fold shown in bold.

While fold-averaged performance summarizes central tendency, it obscures whether differences are driven by a few cases or are sustained across all shoes. To examine this more closely, Figure 10 compares the performance of our model against competing approaches on a shoe-by-shoe basis for the held-out shoes in Fold 3.

In Figure 10a, shoes are ordered along the horizontal axis according to increasing performance under our method. Our model consistently outperforms the uniform baseline and exhibits greater robustness than M(a) and M(b), both of which show a much steeper decline in performance in the lower tail. Moreover, our method outperforms M(a) on more than 90 percent of shoes. Although there is some correlation between the performance of our method and M(b), our approach yields superior performance for the vast majority of shoes. This robustness is further illustrated in Figure 10b, which compares the empirical quantiles of the performance metric across all four methods. Across nearly the entire range of quantiles, our method dominates the competing approaches.

For clarity of visualization, M(Variant A) was omitted from Figure 10. Its performance is visually very similar to that of our method, though slightly worse on average, as shown in

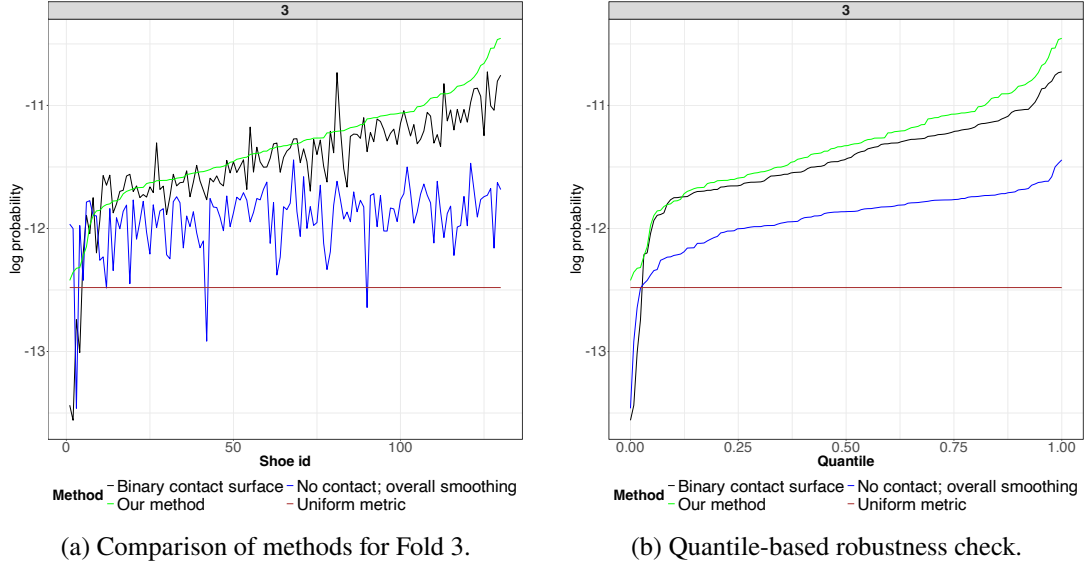


Fig 10: A comparison of four models from Table 1 according to (9) on the individual shoes in cross-validation Fold 3. In (a), the shoes are ordered identically according to increasing performance of Our method. In (b), the quantiles of performance are compared by ordering each method individually.

Table 2. Nevertheless, Our method outperforming M(Variant A) demonstrates the utility of parsimony and feature engineering: despite having far fewer parameters, Our method leverages important information in the image gradient to improve average performance.

To further compare our model against closely related alternatives, Table 3 reports average performance across the ten folds for the model variants described in Table 1. Performance is very similar across these models, particularly among M(Final), M(Variant C), and M(Variant D). Although M(Final) is the top performer in a plurality of folds, M(Variant C) and M(Variant D) exhibit marginally better average performance across folds. In contrast, M(Variant A) is consistently outperformed by the other variants, further demonstrating the utility of incorporating image gradient information into the model.

Fold	M(Final)/Our Method IG, PI, and interaction SV	IG and PI; SV M(variant D)	PI; SV M(variant C)	Only overall Smoothing M(variant B)	15 SV M(variant A)
1	-11.31081	-11.31179	-11.31330	-11.31352	-11.34449
2	-11.31446	-11.31259	-11.31331	-11.31343	-11.33637
3	-11.33436	-11.33304	-11.33258	-11.33311	-11.36233
4	-11.29719	-11.29756	-11.29784	-11.29828	-11.32656
5	-11.32610	-11.32652	-11.32515	-11.32537	-11.34773
6	-11.42573	-11.42637	-11.42672	-11.42743	-11.45226
7	-11.35894	-11.35701	-11.35623	-11.35588	-11.38762
8	-11.28722	-11.28781	-11.28896	-11.28934	-11.33064
9	-11.32842	-11.32716	-11.32740	-11.32714	-11.35275
10	-11.36413	-11.36426	-11.36408	-11.36464	-11.39468
Average	-11.33474	-11.33441	-11.33456	-11.33481	-11.36354

TABLE 3

Average performance of model variants as measured by (9) across ten folds. Top performer for each fold shown in bold. Models variants formulated as in Table 1.

Given the very similar predictive performance of M(Final), M(variant D), and M(variant C), selecting a single recommended specification is not straightforward based exclusively

on average cross-validation performance. The performance differences among these models are small in magnitude and vary slightly across folds. We therefore supplement the fold-averaged comparison with an additional metric designed to assess typical relative per-accidental performance at the level of individual shoes.

Specifically, we introduce the median performance loss ratio, which compares two any models M_1 and M_2 according to

$$\mathcal{R}_M(M_1, M_2) = 100 \times \text{median}_{s \in S} \left(\frac{\exp(m(Y_s = y_s | C_s, M_1))}{\exp(m(Y_s = y_s | C_s, M_2))} \right)$$

where $m(Y_s = y_s | C_s, M)$ is defined in (equation 9), using the parameter θ estimated using the same 10-fold cross-validation procedure described above. This quantity measures the typical per-accidental predictive loss incurred by choosing M_1 in place of M_2 . A value of 100 indicates parity in median performance, values below 100 indicate inferior performance of M_1 relative to M_2 , and values above 100 indicate superior performance of M_1 .

Table 4 reports this metric for each competing model from Table 1, using M(Final) as the reference model M_2 . The results show that M(Final) dominates all baseline and variant models. In particular, models that exclude contact surface information exhibit dramatic losses in median per-accidental predictive performance, with the binary contact surface of [Spencer and Murray \(2020\)](#) and M(Variant A) also having demonstrably worse performance.

Method (M_1)	$\mathcal{R}_M(M_1, M_2)$ (%)
Intercept + PI + IG + interaction SV (M(Final))	1.00×10^2
Intercept and PI SV (M(variant C))	$.998 \times 10^2$
Only intercept SV (M(variant B))	$.998 \times 10^2$
Intercept, IG and PI SV (M(variant D))	$.994 \times 10^2$
15 SV (excluding IG) (M(variant A))	$.648 \times 10^2$
Binary contact surface (M(b))	$.13 \times 10^2$
No contact; overall smoothing (M(a))	2.3×10^{-3}
Uniform metric	3.7×10^{-9}

TABLE 4

median performance loss ratios comparing each method (M_1) against the proposed method M(Final). Values below 100 indicate inferior performance relative to M(Final), while values equal to 100 indicate parity.

Among the closely related variants—M(variant D), M(variant C), and M(variant B)—median performance ratios are close to 100, indicating broadly comparable predictive behavior. Nevertheless, M(Final) attains the highest median performance while maintaining a small set of spatially varying coefficients related to pixel intensity and image gradients. In contrast, M(variant A), which relies on a substantially larger number of spatially varying coefficients but excludes image gradient information, performs consistently worse across metrics.

Taken together, these results motivate our choice of M(Final) as the preferred specification. Although its average predictive performance differs only marginally from that of M(variant D) and M(variant C), M(Final) offers a balance between predictive accuracy, interpretability, and parsimony. In particular, the inclusion of spatially varying image gradient effects provides additional explanatory insight into how the impact of the contact surface varies in space, as illustrated in Figure 4, without incurring the complexity associated with high-dimensional spatial coefficient models. For these reasons, we adopt M(Final) as our recommended model for estimating reliable random match probabilities in forensic footwear analysis.

8. Conclusion

In this work, we developed a Bayesian spatial point process model for the distribution of accidental locations on footwear outsoles conditional on their contact surface. Our primary objective was to support the reliable estimation of accidental-based random match probabilities, which play a key role in interpreting forensic footwear evidence. Building on earlier work by [Spencer and Murray \(2020\)](#), we reformulated this problem within a latent Gaussian model framework, enabling scalable Bayesian inference while simultaneously expanding the class of models that can be practically considered. Novel contributions of this study include considering a continuous-valued version of the contact surface image rather than a thresholded one, allowing the impact of the contact surface to vary spatially, and the inclusion of a novel image gradient terms such that our model specifically accounted for edges.

We validated this framework using the WVU footwear database ([Speir et al., 2016](#)), which is over three times as large as than the JESA database employed by [Spencer and Murray \(2020\)](#). Our recommended specification consistently outperformed existing approaches in the literature as measured by predictive performance on held-out data. Importantly, this superior performance was not confined to a small subset of shoes; our model demonstrated superior robustness in the lower tail, where unreliable estimates pose the greatest forensic risk.

Despite these advances, several limitations remain before such models can be deployed directly in routine forensic casework. Our analysis relied on high-quality laboratory-generated impressions with precisely measured accidental locations. In practice, crime scene impressions are often partial and noisy, with only a subset of accidentals detectable. Understanding how probability models trained on laboratory data translate to these more challenging conditions remains an open problem. Recent work by [Smale and Speir \(2024a,b\)](#) represents important progress in this direction, but further study is needed to further bridge this gap.

There are also several promising methodological extensions. Alternative registration schemes, such as the polar-coordinate approaches proposed by [Richetelli and Speir \(2022\)](#), could potentially lead to further improvement when incorporated within the latent Gaussian framework. Additional pre-processing steps, including standardization of pixel intensity across shoes, may further improve data pooling. Finally, while our current model assumes linear effects of covariates on accidental intensity, nonlinear extensions using generalized additive models or spline-based approaches ([Hastie and Tibshirani, 1986](#); [Perperoglou et al., 2019](#)), as well as clustered point process models such as Neyman–Scott processes [Wang et al. \(2024\)](#), represent natural avenues for future research.

Overall, this work further demonstrates that modern Bayesian spatial modeling tools can substantially improve the estimation of accidental-based random match probabilities in forensic footwear analysis. By combining scalable computation with a large database, the proposed framework provides a principled foundation for future methodological development and, ultimately, for more reliable assessment of forensic footwear evidence in forensic practice.

9. Acknowledgment

We sincerely thank Jacqueline A. Speir for providing the forensic shoeprint dataset used in this study, as well as helpful guidance and feedback. We acknowledge the continuous support from the INLA developers during the implementation and experimentation with different models. We also acknowledge the generous support of the University of Connecticut High Performance Computing (HPC) facilities and sincerely thank its maintainers for ensuring a stable and efficient computing environment for our intensive calculations.

10. Appendix

We divide the appendix in the following sections:

1. In the section 10.1, we described the detailed procedure that is used to evaluate the posterior parameter inference using integrated nested Laplace approximation (INLA).
2. In section 10.2, we described our interest of multinomial probability for each held-out shoes.
3. To avoid the numerical error we described our procedure for the Multinomial probability mass function in the section 10.3.
4. Additional discussion on the comparison metric is provided in the section 10.4.
5. In the section 10.5, we provide a detailed description of the different models that we used for comparison with our proposed model in the Table 5 for the convenience of the readers (Table 1 in main paper).
6. We provide some literature review on the forensic modeling of accidentals in the section 11.
7. We used an important feature image gradient which determines the sharp edges in the shoe print. A description for image gradient/sobel is given in the section 12.
8. We summarized our results in the section 7 of our main paper. In addition, we would like to provide additional summary of the results in the Table 6, 7, and 8 for the validation of the performance of our model. Table 6 describes the average performance across different methods, whereas Table 7, and 8 describes the median based comparison among different competitive methods described in the Table 1 in the main document (Table 5).
9. Finally, in the section 14, we plot the additional diagrams for comparison with our proposed model.

Recall that the main model was defined as

- (10) $Y_{s,a} | \mathcal{N}_a^s, I_a^s, (\beta_{o_1}^{\text{contact}}, \beta_s^{\text{shoe}}, \beta_{a,o_2}^{\text{spatial}}) \sim \text{Pois}(\lambda_{s,a}); s \in \mathcal{S}, a \in \mathcal{A};$
- (11) $x_{s,a}^{\mathbf{i}} = (C_{s,ij})^{i_1} (C_{s,(i-1)j})^{i_2} (C_{s,(i+1)j})^{i_3} (C_{s,i(j-1)})^{i_4} (C_{s,i(j+1)})^{i_5} (I_{s,ij})^{i_6}; \quad \mathbf{i} \in \{0, 1\}^6;$
- (12) $\log(\lambda_{s,a}) = \beta_a^{\text{smooth}} + \beta_s^{\text{shoe}} + \sum_{\mathbf{i} \in \mathcal{I}, \mathcal{I}^* \subseteq \mathcal{I}} x_{s,a}^{\mathbf{i}} (\beta_f^{\mathbf{i}} + \beta_{sv,a}^{\mathbf{i}} \mathbf{1}(\mathbf{i} \in \mathcal{I}^*)); \quad \mathcal{I} \subseteq \{0, 1\}^6.$

We can write down the likelihood as

$$(13) \quad \prod_{s=1}^{|\mathcal{S}|} \mathbb{P}(\mathbf{Y}_s = \mathbf{y}_s | C_s, \boldsymbol{\theta}) = \prod_{s=1}^{|\mathcal{S}|} \prod_{a \in \mathcal{A}} \mathbb{P}(Y_{s,a} = y_{s,a} | \mathcal{N}_a^s, \boldsymbol{\theta}) = \prod_{s=1}^{|\mathcal{S}|} \prod_{a \in \mathcal{A}} \frac{e^{-\lambda_{s,a}} \lambda_{s,a}^{y_{s,a}}}{y_{s,a}!}.$$

Following the notation of Rue, Martino and Chopin (2009), the latent Gaussian field is defined as

$$\mathbf{x} = \left((\beta_a^{\text{smooth}})_{a \in \mathcal{A}}, (\beta_s^{\text{shoe}})_{s \in \mathcal{S}}, (\beta_f^{\mathbf{i}})_{\mathbf{i} \in \mathcal{I}}, (\beta_{sv,a}^{\mathbf{i}})_{a \in \mathcal{A}, \mathbf{i} \in \mathcal{I}^*} \right)^\top.$$

The linear predictor for observation (s, a) is given by

$$\eta_{s,a} = \beta_a^{\text{smooth}} + \beta_s^{\text{shoe}} + \sum_{\mathbf{i} \in \mathcal{I}} x_{s,a}^{\mathbf{i}} \beta_f^{\mathbf{i}} + \sum_{\mathbf{i} \in \mathcal{I}^*} x_{s,a}^{\mathbf{i}} \beta_{sv,a}^{\mathbf{i}},$$

where $\log(\lambda_{s,a}) = \eta_{s,a}$. Let $\boldsymbol{\psi} = (\tau, \tau_{sm}, \{\tau_i\}_{i \in \mathcal{I}^*})$ denote the collection of hyperparameters. Then, up to proportionality,

$$(14) \quad \pi(\mathbf{x} | \mathbf{y}, \boldsymbol{\psi}) \propto \prod_{s \in \mathcal{S}} \prod_{a \in \mathcal{A}} \exp(y_{s,a} \eta_{s,a} - e^{\eta_{s,a}}) \times \exp\left(-\frac{1}{2} \mathbf{x}^\top \mathbf{Q}(\boldsymbol{\psi}) \mathbf{x}\right),$$

where the precision matrix $\mathbf{Q}(\psi)$ is block diagonal with blocks

$$\mathbf{Q}(\psi) = \text{diag}(\tau_{sm}\mathbf{Q}_{sm}, \tau\mathbf{I}, \mathbf{Q}(\beta_f), \{\tau_i\mathbf{Q}_i\}_{i \in \mathcal{I}^*}).$$

The latent Gaussian field is given by $\mathbf{x} = \boldsymbol{\theta}$. Recall, β^{shoe} is a nuisance parameter. The posterior for $\boldsymbol{\theta} \setminus \{\beta^{\text{shoe}}\}$ given the data := $\left\{ \{\mathbf{Y}_s = \mathbf{y}_s\}_{s=1}^S, \{C_s\}_{s=1}^S \right\}$ and hyperparameter ψ can be expressed as likelihood \times prior given hyperparameter, i.e.

$$\begin{aligned} \pi(\boldsymbol{\theta} \setminus \{\beta^{\text{shoe}}\} | \text{data}, \psi) &\propto \pi(\text{data} | \boldsymbol{\theta} \setminus \{\beta^{\text{shoe}}\}) \pi(\boldsymbol{\theta} \setminus \{\beta^{\text{shoe}}\} | \psi) \\ &\propto \prod_{s=1}^{|S|} \left\{ \int_{\beta_s^{\text{shoe}}} \prod_{a \in \mathcal{A}} \mathbb{P}(Y_{s,a} = y_{s,a} | C_s, \boldsymbol{\theta}) \pi(\beta_s^{\text{shoe}} | \tau) d\beta_s^{\text{shoe}} \right\} \\ &\quad \times \pi(\beta_f | Q_f) \pi(\beta^{\text{smooth}} | \mathbf{Q}_{sm}) \pi(\beta_{sv} | \mathbf{Q}_j; j = 1, \dots, |\mathcal{I}^*|) \\ &= \prod_{s=1}^{|S|} \left\{ \int_{\beta_s^{\text{shoe}}} \prod_{a \in \mathcal{A}} \frac{e^{-\lambda_{s,a}} \lambda_{s,a}^{y_{s,a}}}{y_{s,a}!} \frac{\sqrt{\tau}}{\sqrt{2\pi}} \exp\left(-\frac{\tau(\beta_s^{\text{shoe}})^2}{2}\right) d\beta_s^{\text{shoe}} \right\} \\ &\quad \times \frac{|Q_f|^{1/2}}{(2\pi)^{(|\mathcal{I}|+1)/2}} \exp\left(-\frac{(\beta_f)^\top Q_f(\beta_f)}{2}\right) \\ &\quad \times \frac{|\tau_{sm}\mathbf{Q}_{sm}|^{1/2}}{(2\pi)^{|\mathcal{A}|/2}} \exp\left(-\frac{\tau_{sm}}{2} (\beta^{\text{smooth}})^\top \mathbf{Q}_{sm} (\beta^{\text{smooth}})\right) \\ &\quad \times \prod_{j=1}^{|\mathcal{I}^*|} \frac{(\tau_j |\mathbf{Q}_j|)^{1/2}}{(2\pi)^{|\mathcal{A}|/2}} \exp\left(-\frac{\tau_j}{2} (\beta_{sv}^j)^\top \mathbf{Q}_j (\beta_{sv}^j)\right). \end{aligned}$$

10.1. INLA procedure

Our goal is to come up with a point estimate of the parameters. We need to compute the full posterior and/or marginal posterior expectations. Markov Chain Monte Carlo (MCMC) is a powerful statistical technique used for sampling from complex probability distributions. However, it has its challenges and potential issues, for example, convergence issues due to poor choice of initial values, autocorrelation, burn-in period identification, etc. Moreover, MCMC can be computationally intensive, especially for large datasets or high-dimensional parameter spaces. Integrated Nested Laplace Approximation (INLA) is an advanced statistical method that provides a computationally efficient alternative to traditional Markov Chain Monte Carlo (MCMC) methods for Bayesian inference. INLA is employed when exact Bayesian inference is computationally challenging, especially in cases involving high-dimensional and hierarchical models. It combines Laplace approximation with numerical integration techniques to provide fast and accurate approximations of posterior distributions. We are implementing INLA for computational advantage and estimation of the parameters. For computational advantage in INLA, one small error term $\epsilon \sim \mathcal{N}(0, \tau_\epsilon^2)$ is added in link function 12. It can relax the assumption of independence of the prior. If $\tau_\epsilon^2 = 0$, we can shift to the independence assumption of prior, which we assumed for calculating posterior in (15). By choosing INLA will not attempt to estimate the previous posterior distribution mentioned in (15) but the marginals of the parameters $\boldsymbol{\theta}$ for individual component θ_i and hyperparameters ψ for individual component ψ_k . So we need to calculate marginal posteriors, which are:

$$(15) \quad p(\theta_i | \mathbf{y}) = \int p(\theta_i | \mathbf{y}, \psi) p(\psi | \mathbf{y}) d\psi;$$

$$(16) \quad p(\psi_k | \mathbf{y}) = \int p(\psi | \mathbf{y}) d\psi_{-k}.$$

To compute the above we need to calculate $p(\psi | \mathbf{y})$ and $p(\theta_i | \mathbf{y}, \psi)$. To calculate $p(\psi | \mathbf{y})$ we observe that we can approximate it with the Gaussian approximation of $p(\theta | \psi, \mathbf{y})$ as $\tilde{p}(\theta | \psi, \mathbf{y})$ at the estimated mode of $p(\theta | \mathbf{y}, \psi)$ which is $\theta^*(\psi) := \operatorname{argmax}_{\theta} p(\theta | \psi, \mathbf{y})$. One can express

$$(17) \quad \log(p(\theta | \mathbf{y}, \psi)) = \log(p(\mathbf{y} | \theta, \psi)) + \log(p(\theta | \psi)) + \text{constant}.$$

Now one should compute the Taylor series expansion of $f(\theta) = \log(p(\mathbf{y} | \theta, \psi))$ around $\theta^*(\psi)$ and approximate with Gaussian distribution with precision matrix as $Q(\theta) + c(\theta)$ where $c(\theta)$ contains negative second derivative at $\theta^*(\psi)$ with respect to θ and the mean parameter is $\theta^*(\psi)$. Observe that,

$$(18) \quad p(\psi | \mathbf{y}) = \frac{p(\theta, \psi | \mathbf{y})}{p(\theta | \psi, \mathbf{y})} \propto \frac{p(\mathbf{y} | \theta) p(\theta | \psi) p(\psi)}{p(\theta | \psi, \mathbf{y})} \approx \frac{p(\mathbf{y} | \theta) p(\theta | \psi) p(\psi)}{\tilde{p}(\theta | \psi, \mathbf{y})} \Big|_{\theta=\theta^*(\psi)} := \tilde{p}(\psi | \mathbf{y}).$$

The other integration is also calculated similarly as follows. We also approximate $p(\theta_i | \theta_i, \psi, \mathbf{y})$ by $\tilde{p}(\theta_{-i} | \theta_i, \psi, \mathbf{y})$ at the estimated mode $\theta_{-i}^*(\theta_i, \psi)$.

$$(19) \quad p(\theta_i | \mathbf{y}, \psi) = \frac{p((\theta_i, \theta_{-i}) | \mathbf{y}, \psi)}{p(\theta_{-i} | \theta_i, \psi, \mathbf{y})} \propto \frac{p((\theta_i, \theta_{-i}) | \mathbf{y}, \psi)}{\tilde{p}(\theta_{-i} | \theta_i, \psi, \mathbf{y})} \Big|_{\theta_{-i}=\theta_{-i}^*(\theta_i, \psi)} := \tilde{p}(\theta_i | \mathbf{y}, \psi).$$

Now, finally, we do calculate a numerical integration to calculate $p(\theta_i | \mathbf{y})$.

$$(20) \quad p(\theta_i | \mathbf{y}) \approx \sum_{k=1}^K \tilde{p}(\theta_i | \mathbf{y}, \psi_k) \tilde{p}(\psi_k | \mathbf{y}) \Delta_k,$$

where K is the number of hyperparameters with their corresponding weights Δ_k for $k = 1, \dots, K$. A complete and detailed description can be found in [Blangiardo et al. \(2013\)](#), [Rue et al. \(2017\)](#), e.t.c.

INLA is capable of handling up to ten spatially varying coefficients while estimating the precision parameter. If the model has more than ten spatially varying coefficients, we fixed the value of the precision parameter that we obtained through empirical Bayes.

10.2. Multinomial Poisson likelihood

Recall that,

$$\eta_{s,a} = \beta_a^{\text{smooth}} + \beta_s^{\text{shoe}} + \sum_{\mathbf{i} \in \mathcal{I}} x_{s,a}^{\mathbf{i}} \beta_f^{\mathbf{i}} + \sum_{\mathbf{i} \in \mathcal{I}^*} x_{s,a}^{\mathbf{i}} \beta_{sv,a}^{\mathbf{i}}.$$

We can decompose $\eta_{s,a} = \eta_{s,a}^1 + \beta_s^{\text{shoe}}$, where

$$\eta_{s,a}^1 = \beta_a^{\text{smooth}} + \sum_{\mathbf{i} \in \mathcal{I}} x_{s,a}^{\mathbf{i}} \beta_f^{\mathbf{i}} + \sum_{\mathbf{i} \in \mathcal{I}^*} x_{s,a}^{\mathbf{i}} \beta_{sv,a}^{\mathbf{i}}.$$

Now if we marginalize $\mathbb{P}(\mathbf{Y}_s = \mathbf{y}_s | C_s, C_{S_T}, \tau = \hat{\tau})$ over the distribution β_s^{shoe} , we obtain the following:

$$\begin{aligned} & \mathbb{E}_{\beta_s^{\text{shoe}}} [\mathbb{P}(\mathbf{Y}_s = \mathbf{y}_s | C_s, C_{S_T}, \tau = \hat{\tau})] \\ &= \int_{-\infty}^{+\infty} \prod_{a \in \mathcal{A}} \frac{\exp(-\lambda_{s,a})(\lambda_{s,a})^{y_{s,a}}}{y_{s,a}!} \mathcal{P}(\beta_s^{\text{shoe}}) d\beta_s^{\text{shoe}} \\ &= \int_{-\infty}^{+\infty} \frac{\exp(-\sum_{a \in \mathcal{A}} \exp(\eta_{s,a}^1 + \beta_s^{\text{shoe}})) (\prod_{a \in \mathcal{A}} \exp(\eta_{s,a}^1 + \beta_s^{\text{shoe}})^{y_{s,a}})}{\prod_{a \in \mathcal{A}} y_{s,a}!} \mathcal{P}(\beta_s^{\text{shoe}}) d\beta_s^{\text{shoe}} \end{aligned}$$

$$\begin{aligned}
&= \int_{-\infty}^{+\infty} \frac{\exp(-\sum_{a \in \mathcal{A}} \exp(\eta_{s,a}^1 + \beta_s^{\text{shoe}}))}{\prod_{a \in \mathcal{A}} y_{s,a}!} \times \\
&\quad \times \left(\sum_{a \in \mathcal{A}} \exp(\eta_{s,a}^1 + \beta_s^{\text{shoe}}) \right)^{N_s} \prod_{a \in \mathcal{A}} \frac{\exp(\eta_{s,a}^1 + \beta_s^{\text{shoe}})^{y_{s,a}}}{(\sum_{a \in \mathcal{A}} \exp(\eta_{s,a}^1 + \beta_s^{\text{shoe}}))^{y_{s,a}}} \mathcal{P}(\beta_s^{\text{shoe}}) d\beta_s^{\text{shoe}} \\
&= \int_{-\infty}^{+\infty} \frac{\exp(-\sum_{a \in \mathcal{A}} \exp(\eta_{s,a}^1 + \beta_s^{\text{shoe}})) (\sum_{a \in \mathcal{A}} \exp(\eta_{s,a}^1 + \beta_s^{\text{shoe}}))^{N_s}}{N_s!} \times \\
&\quad \times \frac{N_s!}{\prod_{a \in \mathcal{A}} y_{s,a}!} \prod_{a \in \mathcal{A}} \frac{\exp(\eta_{s,a}^1 + \beta_s^{\text{shoe}})^{y_{s,a}}}{(\sum_{a \in \mathcal{A}} \exp(\eta_{s,a}^1 + \beta_s^{\text{shoe}}))^{y_{s,a}}} \mathcal{P}(\beta_s^{\text{shoe}}) d\beta_s^{\text{shoe}},
\end{aligned}$$

where $\sum_{a \in \mathcal{A}} y_{s,a} = N_s$; hence in the third equality we obtain

$$\prod_{a \in \mathcal{A}} \left(\sum_{a \in \mathcal{A}} \exp(\eta_{s,a}^1 + \beta_s^{\text{shoe}}) \right)^{y_{s,a}} = \left(\sum_{a \in \mathcal{A}} \exp(\eta_{s,a}^1 + \beta_s^{\text{shoe}}) \right)^{N_s}.$$

The function inside integration can be seen as product of three parts. The first part is Poisson distribution at point N_s with parameter

$$(21) \quad \sum_{a \in \mathcal{A}} \exp(\eta_{s,a}^1 + \beta_s^{\text{shoe}}) = \exp(\beta_s^{\text{shoe}}) \sum_{a \in \mathcal{A}} \exp(\eta_{s,a}^1).$$

The second part can be thought of a multinomial distribution with parameters $(N_s, \{\pi_a\}) := \left\{ \frac{\exp(\eta_{s,a}^1 + \beta_s^{\text{shoe}})^{y_{s,a}}}{(\sum_{a \in \mathcal{A}} \exp(\eta_{s,a}^1 + \beta_s^{\text{shoe}}))^{y_{s,a}}} \right\}; a \in \mathcal{A}$. The third part is $\mathcal{P}(\beta_s^{\text{shoe}}) \sim N(0, \frac{1}{\tau})$. Now if we observe closely the probabilities for multinomial distribution in second part, they are independent of β_s^{shoe} as from both numerator and denominator of $\frac{\exp(\eta_{s,a}^1 + \beta_s^{\text{shoe}})^{y_{s,a}}}{(\sum_{a \in \mathcal{A}} \exp(\eta_{s,a}^1 + \beta_s^{\text{shoe}}))^{y_{s,a}}}$; $\exp(\beta_s^{\text{shoe}})^{y_{s,a}}$ will be canceled out. Hence, we can write it as:

$$(22) \quad \frac{\exp(\eta_{s,a}^1 + \beta_s^{\text{shoe}})^{y_{s,a}}}{(\sum_{a \in \mathcal{A}} \exp(\eta_{s,a}^1 + \beta_s^{\text{shoe}}))^{y_{s,a}}} = \frac{\exp(\eta_{s,a}^1)^{y_{s,a}} \exp(\beta_s^{\text{shoe}})^{y_{s,a}}}{(\sum_{a \in \mathcal{A}} \exp(\eta_{s,a}^1))^{y_{s,a}} \exp(\beta_s^{\text{shoe}})^{y_{s,a}}}$$

$$(23) \quad = \frac{\exp(\eta_{s,a}^1)^{y_{s,a}}}{(\sum_{a \in \mathcal{A}} \exp(\eta_{s,a}^1))^{y_{s,a}}}.$$

We can therefore take the multinomial part outside the integration and calculate the integration over β_s^{shoe} for the Poisson distribution.

10.3. Multinomial PMF evaluation

In the multinomial PMF, we have to multiply over a large number of probabilities which do cause numerical error. To deal with this problem, we used *logSumExp* trick. For the second part we calculate the multinomial probability in log scale. For calculating integration we take a large possible range of β_s^{shoe} and subdivide the range in D many parts as $\beta_{s,1}^{\text{shoe}}, \beta_{s,2}^{\text{shoe}}, \dots, \beta_{s,D}^{\text{shoe}}$ each of Δ length. Now the first part and third part can be evaluated for each segment $\beta_{s,d}^{\text{shoe}}$ and then if we multiply by Δ and sum over each segments the integration can be approximated.

$$\begin{aligned}
&\int_{-\infty}^{+\infty} \frac{\exp(-\sum_{a \in \mathcal{A}} \exp(\eta_{s,a}^1 + \beta_s^{\text{shoe}})) (\sum_{a \in \mathcal{A}} \exp(\eta_{s,a}^1 + \beta_s^{\text{shoe}}))^{N_s}}{N_s!} \times \\
&\quad \times \frac{N_s!}{\prod_{a \in \mathcal{A}} y_{s,a}!} \prod_{a \in \mathcal{A}} \frac{\exp(\eta_{s,a}^1)}{\sum_{a \in \mathcal{A}} \exp(\eta_{s,a}^1)} \mathcal{P}(\beta_s^{\text{shoe}}) d\beta_s^{\text{shoe}}
\end{aligned}$$

$$\begin{aligned}
&= \frac{N_s!}{\prod_{a \in \mathcal{A}} y_{s,a}!} \prod_{a \in \mathcal{A}} \frac{\exp(\eta_{s,a}^1)}{\sum_{a \in \mathcal{A}} \exp(\eta_{s,a}^1)} \times \\
&\quad \times \int_{-\infty}^{+\infty} \frac{\exp(-\sum_{a \in \mathcal{A}} \exp(\eta_{s,a}^1 + \beta_s^{\text{shoe}})) (\sum_{a \in \mathcal{A}} \exp(\eta_{s,a}^1 + \beta_s^{\text{shoe}}))^{N_s}}{N_s!} \mathcal{P}(\beta_s^{\text{shoe}}) d\beta_s^{\text{shoe}}.
\end{aligned}$$

Now let us define $\nu_{s,a,d} := \eta_{s,a}^1 + \beta_{s,d}^{\text{shoe}}$ as the value of the parameter when it is being evaluated at a specific segment $\beta_{s,d}^{\text{shoe}}$.

$$\begin{aligned}
&\log \left(\int_{-\infty}^{+\infty} \frac{\exp \left(-\sum_{a \in \mathcal{A}} \exp(\eta_{s,a}^1 + \beta_s^{\text{shoe}}) \right) \left(\sum_{a \in \mathcal{A}} \exp(\eta_{s,a}^1 + \beta_s^{\text{shoe}}) \right)^{N_s}}{N_s!} \mathcal{P}(\beta_s^{\text{shoe}}) d\beta_s^{\text{shoe}} \right) \\
&\approx \log \left(\sum_{d=1}^D \frac{\exp \left(-\sum_{a \in \mathcal{A}} \exp(\nu_{s,a,d}) \right) \left(\sum_{a \in \mathcal{A}} \exp(\nu_{s,a,d}) \right)^{N_s}}{N_s!} \mathcal{P}(\beta_{s,d}^{\text{shoe}}) \Delta \right) \\
&= \log \left(\sum_{d=1}^D \exp \left(\log \left\{ \frac{\exp \left(-\sum_{a \in \mathcal{A}} \exp(\nu_{s,a,d}) \right) \left(\sum_{a \in \mathcal{A}} \exp(\nu_{s,a,d}) \right)^{N_s}}{N_s!} \mathcal{P}(\beta_{s,d}^{\text{shoe}}) \Delta \right\} \right) \right) \\
&= \log \left(\sum_{d=1}^D \exp \left(\log \left\{ \frac{\exp \left(-\sum_{a \in \mathcal{A}} \exp(\nu_{s,a,d}) \right) \left(\sum_{a \in \mathcal{A}} \exp(\nu_{s,a,d}) \right)^{N_s}}{N_s!} \mathcal{P}(\beta_{s,d}^{\text{shoe}}) \right\} \right) \right) \\
&\quad + \log(\Delta) \\
&= \log \left(\sum_{d=1}^D \exp \left(\log \left\{ \frac{\exp \left(-\sum_{a \in \mathcal{A}} \exp(\nu_{s,a,d}) \right) \left(\sum_{a \in \mathcal{A}} \exp(\nu_{s,a,d}) \right)^{N_s}}{N_s!} \right\} \right) \right) \\
&\quad + \log \left(\mathcal{P}(\beta_{s,d}^{\text{shoe}}) \right) + \log(\Delta).
\end{aligned}$$

We have 1300 shoes, which include both right and left shoes flipped to the right. We made 10 fold cross-validation. So for each fold of the held-out data, we have 130 shoes. We already defined the second part which can be thought of a multinomial distribution with parameters $(N_s, \{\pi_a\}) := \left\{ \frac{\exp(\eta_{s,a}^1 + \beta_s^{\text{shoe}})^{y_{s,a}}}{(\sum_{a \in \mathcal{A}} \exp(\eta_{s,a}^1 + \beta_s^{\text{shoe}}))^{y_{s,a}}} \right\}; a \in \mathcal{A}$. Hence, for each shoe in the held-out data for each fold of the cross-validation, we can calculate the following:

$$\frac{N_s!}{\prod_{a \in \mathcal{A}} y_{s,a}!} \prod_{a \in \mathcal{A}} \frac{\exp(\eta_{s,a}^1 + \beta_s^{\text{shoe}})^{y_{s,a}}}{(\sum_{a \in \mathcal{A}} \exp(\eta_{s,a}^1 + \beta_s^{\text{shoe}}))^{y_{s,a}}} = \frac{N_s!}{\prod_{a \in \mathcal{A}} y_{s,a}!} \prod_{a \in \mathcal{A}} \frac{\exp(\eta_{s,a}^1)^{y_{s,a}}}{(\sum_{a \in \mathcal{A}} \exp(\eta_{s,a}^1))^{y_{s,a}}},$$

where β_a can be estimated from the rest of the 1300 – 130 shoes. For comparison, we do not consider the constant part in the multinomial probability for held-out data,

$$\tilde{p}_{m,s} := \prod_{a \in \mathcal{A}} \frac{\exp(\eta_{s,a}^1)^{y_{s,a}}}{(\sum_{a \in \mathcal{A}} \exp(\eta_{s,a}^1))^{y_{s,a}}}; s \in \mathcal{S}_{T^c}.$$

Now, when we consider all cross-validation, we get this result for all shoes, i.e. $\tilde{p}_{m,s}$ and transfer it to log scale $\log(\tilde{p}_{m,s})$. We have also calculated the Poisson probability after integrating out the shoe effect, i.e.,

$$\tilde{p}_{p,s} := \int_{-\infty}^{+\infty} \frac{\exp(-\sum_{a \in \mathcal{A}} \exp(\eta_{s,a}^1 + \beta_s^{\text{shoe}})) (\sum_{a \in \mathcal{A}} \exp(\eta_{s,a}^1 + \beta_s^{\text{shoe}}))^{N_s}}{N_s!} \mathcal{P}(\beta_s^{\text{shoe}}) d\beta_s^{\text{shoe}}$$

for $s \in \mathcal{S}_{T^c}$ and we can transfer it to log scale $\log(\tilde{p}_{p,s})$.

10.4. Comparison metric

From the above section, we can write:

$$\tilde{p}_{m,s} = \prod_{a \in \mathcal{A}} (q_{sa}(C_s, \theta_M))^{y_{s,a}},$$

where

$$q_{sa}(C_s, \theta_M) = \frac{\exp(\sum_{i \in \mathcal{I}} x_{s,a}^i \beta_f^i + \sum_{i \in \mathcal{I}^*} x_{s,a}^i \beta_{sv,a}^i + \beta_a^{\text{smooth}})}{(\sum_{a \in \mathcal{A}} \exp(\sum_{i \in \mathcal{I}} x_{s,a}^i \beta_f^i + \sum_{i \in \mathcal{I}^*} x_{s,a}^i \beta_{sv,a}^i + \beta_a^{\text{smooth}}))}.$$

We described our interest in multinomial probability for each held-out shoe. Now for a held-out shoe s , we know the accidental count for each of the grid, $y_{s,a}; a \in \mathcal{A}$. Now, for a method M , we do estimate the multinomial probability $q_{sa}(C_s, \theta_M)$. So the multinomial probability will be,

$$L(y_{s,a}; q_{sa}(C_s, \theta_M)) = \frac{N_s!}{\prod_{a \in \mathcal{A}} y_{s,a}!} \prod_{a \in \mathcal{A}} (q_{sa}(C_s, \theta_M))^{y_{s,a}}.$$

Hence, the log-likelihood will be,

$$\log L(y_{s,a}; q_{sa}(C_s, \theta_M)) = \log(N_s!) - \sum_{a \in \mathcal{A}} \log(y_{s,a}!) + \sum_{a \in \mathcal{A}} y_{s,a} \log(q_{sa}(C_s, \theta_M)).$$

Now observe that, the terms $\log(N_s!)$ and $\sum_{a \in \mathcal{A}} \log(y_{s,a}!)$ are independent of any probability and same for all multinomial based likelihood. So we can avoid these two terms. Now, if we normalize $\log L(y_{s,a}; q_{sa}(C_s, \theta_M))$ by total number of accidentals $\sum_{a \in \mathcal{A}} y_{s,a} = N_s$, we obtain,

$$\frac{\log L(y_{s,a}; q_{sa}(C_s, \theta_M))}{N_s} = \sum_{a \in \mathcal{A}} \frac{y_{s,a}}{\sum_{a \in \mathcal{A}} y_{s,a}} \log(q_{sa}(C_s, \theta_M)).$$

Now for a held-out shoe s , we know the accidental count for each of the grid, $y_{s,a}; a \in \mathcal{A}$. Now for a method M , we do estimate the multinomial probability $q_{sa}(C_s, \theta_M)$. So the multinomial probability will be,

$$L(y_{s,a}; q_{sa}(C_s, \theta_M)) = \frac{N_s!}{\prod_{a \in \mathcal{A}} y_{s,a}!} \prod_{a \in \mathcal{A}} (q_{sa}(C_s, \theta_M))^{y_{s,a}}.$$

Hence, the log-likelihood will be,

$$\log L(y_{s,a}; q_{sa}(C_s, \theta_M)) = \log(N_s!) - \sum_{a \in \mathcal{A}} \log(y_{s,a}!) + \sum_{a \in \mathcal{A}} y_{s,a} \log(q_{sa}(C_s, \theta_M)).$$

Now observe that the terms $\log(N_s!)$ and $\sum_{a \in \mathcal{A}} \log(y_{s,a}!)$ are independent of any probability and the same for all multinomial-based likelihoods. So we can avoid these two terms. Now, if we normalize $\log L(y_{s,a}; q_{sa}(C_s, \theta_M))$ by the total number of accidentals $\sum_{a \in \mathcal{A}} y_{s,a} = N_s$, we obtain,

$$m(Y_s = y_s | C_s) = \frac{\log L(y_{s,a}; q_{sa}(C_s, \theta_M))}{N_s} = \sum_{a \in \mathcal{A}} \frac{y_{s,a}}{\sum_{a \in \mathcal{A}} y_{s,a}} \log(q_{sa}(C_s, \theta_M)).$$

We consider a uniform metric defined as giving a uniform probability across all the grid points. We do not consider any covariate for this model. The metric is:

$$\left(\frac{1}{\text{number of grids}} \right)^{N_s},$$

where $\sum_{a \in \mathcal{A}} y_{s,a} = N_s$ is the total number of accidentals of the s th shoe.

CCC: The Concordance Correlation Coefficient (CCC) is a widely used metric for assessing the agreement between two methods of continuous measurement. For two methods M_1 and M_2 , the CCC evaluates the agreement between

$$p_{M_1} := \{m(Y_s = y_s \mid C_s, M_1) : s \in \mathcal{S}\} \quad \text{and} \quad p_{M_2} := \{m(Y_s = y_s \mid C_s, M_2) : s \in \mathcal{S}\},$$

and is defined as

$$\text{CCC}_{M_1}^{M_2} = \rho_{p_{M_1} p_{M_2}}^{p_{M_2}} \times \frac{2}{\nu + \nu^{-1} + u^2},$$

where $\rho_{p_{M_1} p_{M_2}}^{p_{M_2}}$ denotes the Pearson correlation coefficient between the vectors p_{M_1} and p_{M_2} ,

$$\nu = \frac{s_{p_{M_1}}}{s_{p_{M_2}}}$$

is the ratio of their sample standard deviations, and

$$u = \frac{\mu_{p_{M_1}} - \mu_{p_{M_2}}}{\sqrt{s_{p_{M_1}} s_{p_{M_2}}}}$$

is the standardized difference between their sample means. Here, $\mu_{p_{M_j}}$ and $s_{p_{M_j}}$ denote the sample mean and standard deviation of the vector p_{M_j} , respectively, for $j \in \{1, 2\}$. Additionally, in the Table 9 (section 13), we describe the comparison based on CCC across different methods.

10.5. Detailed description of different models

A detailed description of the methods can also be found in Table 5.

Model	Binary(B) None(\times), Continuous (C)	Description	32 (fixed)	sobel fixed	Spatially varying	sobel spatially varying	Overall smoothing
Uniform	\times	uniform metric	\times	\times	\times	\times	\times
M(a)	\times	spatially varying intercept	\times	\times	\times	\times	\checkmark
M(b)	B	spatially varying intercept and 32 fixed effects (N_a^s with interaction)	\checkmark	\times	\times	\times	\checkmark
M(variant A)	C	spatially varying intercept with 15 spatially varying (upto 2nd order interactions of N_a^s), and 32 fixed effects (N_a^s with interaction)	\checkmark	\times	15 (upto 2nd order)	\times	\checkmark
M(variant B)	C	spatially varying intercept, 64 fixed effect (sobel and N_a^s with interaction)	\checkmark	\checkmark	\times	\times	\checkmark
M(variant C)	C	spatially varying intercept and pixel intensity, 64 fixed effect (sobel and N_a^s with interaction)	\checkmark	\checkmark	1 (pixel intensity)	\checkmark	\checkmark
M(variant D)	C	spatially varying intercept, pixel intensity and sobel; 64 fixed effect (sobel and N_a^s with interaction)	\checkmark	\checkmark	2 (pixel intensity + sobel)	\checkmark	\checkmark
M(Final)	C	spatially varying intercept, pixel intensity, sobel and interaction between sobel and pixel intensity; 64 fixed effect (sobel and N_a^s with interaction)	\checkmark	\checkmark	2 (pixel intensity + pixel intensity * sobel)	\checkmark	\checkmark

TABLE 5
Competitive models and state-of-the-art description

11. Several existing forensics models

Following [Richetelli and Speir \(2022\)](#), let R_a denote the number of randomly acquired characteristics (RACs) observed in spatial bin a of the standardised outsole map. The count data are modelled as a global model:

$$(24) \quad R_a | \lambda \sim \text{Poisson}(\lambda), a = 1, \dots, |\mathcal{A}|.$$

For local model, the considered model was:

$$(25) \quad R_a | \lambda_a \sim \text{Poisson}(\lambda_a), a = 1, \dots, |\mathcal{A}|$$

11.1. Model Based on Tread Contact

[Richetelli and Speir \(2022\)](#) propose a model in which RAC frequency is explained solely by the degree of tread contact. Let C_a denote the average number of contact pixels in bin a , and let B_a denote the bin-partiality offset correcting for non-uniform overlap of the outsole boundary. The log-intensity model is

$$(26) \quad \log(\lambda) = \beta_0 + \beta_1 C_a + \beta_2 \log(B_a).$$

Here β_0 is an intercept, β_1 reflects variation due to contact area, and β_2 adjusts for edge effects introduced by bin coverage.

11.2. Model Based on Contact-Localised Wear

To evaluate the effect of physical use on RAC occurrence, [Richetelli and Speir \(2022\)](#) incorporate categorical wear levels. Let LC_a , MC_a , and HC_a denote the average counts of pixels classified as light, moderate, and high contact-localised wear, respectively. The corresponding Poisson regression is

$$(27) \quad \log(\lambda) = \beta_0 + \beta_1 LC_a + \beta_2 MC_a + \beta_3 HC_a + \beta_4 \log(B_a).$$

The authors report that moderate wear tends to increase RAC accumulation, whereas light and high wear appear to reduce it due to insufficient interaction or abrasion-induced loss.

11.3. Location indexed Coefficient Model

To capture spatial heterogeneity across the outsole surface, [Richetelli and Speir \(2022\)](#) employ a geographically weighted Poisson regression (GWPR). Let (u_a, v_a) denote bin centroids, and let $\beta_k(u_a, v_a)$ denote spatially varying coefficient surfaces. So a general non-homogeneous spatial point process as a follow-up of the models described in equations 26 and 27 are the models in the equation 28 and 29.

$$(28) \quad \log(\lambda_a) = \beta_0(u_a, v_a) + \beta_1 C_a(u_a, v_a) + \beta_2 \log(B_a(u_a, v_a)).$$

Similarly, another spatially varying model can be written as:

$$(29) \quad \log(\lambda_a) = \beta_0(u_a, v_a) + \beta_1 LC_a(u_a, v_a) + \beta_2 MC_a(u_a, v_a) + \beta_3 HC_a(u_a, v_a) + \beta_4 \log(B_a(u_a, v_a)).$$

This formulation allows non-stationarity in both wear effects and induced spatial dependence. Moreover, the intercept term is spatially varying for the models in the equation 28 and 29.

The resulting process assumes constant intensity over contact pixels and serves as a null model for hypothesis testing.

These models explain broad spatial trends by linking RAC frequency to average contact and wear patterns across the outsole. Still, they operate at a population-averaged spatial resolution rather than modeling shoe-specific spatial variability. As a result, the models assume uniform spatial effects across all shoes and employ a global Poisson structure that cannot account for localized clustering, overdispersion, or region-specific mechanisms of RAC formation, thereby limiting their forensic interpretability and sensitivity to fine-grained spatial heterogeneity.

In our models, we considered the neighborhood contact information as a covariate and also included their interactions. We have the shoe-specific model of the contact surface instead of the average contact surface.

12. Image gradient

The Sobel operator or image gradient is a discrete differentiation operator used to compute an approximation of the gradient of the image intensity function. A high-pass filter enhances rapid intensity changes in an image, which correspond to edges and fine details, while suppressing smooth areas with gradual transitions or low frequencies. The Sobel operator uses two convolution kernels, one for detecting changes in the horizontal direction (G_x) and another for detecting changes in the vertical direction (G_y). These kernels are defined as:

$$G_x = \begin{bmatrix} -1 & 0 & 1 \\ -2 & 0 & 2 \\ -1 & 0 & 1 \end{bmatrix}; \quad G_y = G_x^T.$$

Let the horizontal filter produce $(G_{x,a} : \bar{\mathcal{N}}_a^s \times G_x \rightarrow \mathbb{R})$ and the vertical filter produce $(G_{y,a} : \bar{\mathcal{N}}_a^s \times G_y \rightarrow \mathbb{R})$ for all coordinates $a \in \mathcal{A}$.

For computational efficiency, particularly when processing large images or multiple frames, we implement the convolution operations using Fast Fourier Transform (FFT). The convolution theorem states that convolution in the spatial domain is equivalent to element-wise multiplication in the frequency domain:

$$\text{conv}(f, g) = \mathcal{F}^{-1}[\mathcal{F}(f) \cdot \mathcal{F}(g)],$$

where \mathcal{F} denotes the FFT operation. For an image of size $n_x \times n_y$ pixels, this approach reduces the computational complexity from $O(n_x n_y \cdot k^2)$ for direct spatial convolution with a $k \times k$ kernel to $O(n_x n_y \log(n_x n_y))$ for FFT-based convolution (see [Vetterli et al. \(1984\)](#), [Pau et al. \(2010\)](#), e.t.c.). Implementing FFT-based convolution is particularly advantageous for high-resolution images. The horizontal and vertical gradient components are calculated using FFT-based convolution as:

$$G_{x,a} = \mathcal{F}^{-1}[\mathcal{F}(\bar{\mathcal{N}}_a^s) \cdot \mathcal{F}(G_x)], \quad G_{y,a} = \mathcal{F}^{-1}[\mathcal{F}(\bar{\mathcal{N}}_a^s) \cdot \mathcal{F}(G_y)],$$

where $\bar{\mathcal{N}}_a^s$ represents the neighborhood around pixel a , and the convolution operations are efficiently computed using FFT for all coordinates $a \in \mathcal{A}$.

The gradient magnitude at each pixel is then computed as:

$$G_a = \sqrt{G_{x,a}^2 + G_{y,a}^2} \in \mathbb{R}; \quad \forall a \in \mathcal{A}.$$

13. Additional comparative study from other methods

To summarize the results across different folds (Table 1), we present another metric:

$$(30) \quad g(M_2, M_1) := \exp \left(\frac{1}{10} \sum_{i=1}^{10} (P_{S_i}^{M_2} - P_{S_i}^{M_1}) \right) \times 100,$$

for two methods M_1 and M_2 in the Table 6. If $g(M_2, M_1) > 100$, then we have positive gain for choosing the method M_2 over M_1 , and similarly $g(M_2, M_1) < 100$ means M_1 is performing better than M_2 .

Method	Uniform	M(a)(Only overall smoothing)	M(b) (binary)	M(variant A) (Our variant)	Our Method M(Final)
Uniform	100.00	176.92	273.41	305.38	311.30
M(a)	56.52	100.00	154.54	172.62	175.96
M(b)	36.58	64.71	100.00	111.69	113.86
M(variant A)	32.75	57.93	89.53	100.00	101.94
Our method /M(Final)	32.12	56.83	87.83	98.10	100.00

TABLE 6

Average percentage gain of the method in the row method (M_1) compared to the column method (M_2), computed as $g(M_2, M_1)$ (Equation 30). Above 100% means positive gain, and below 100% means negative gain. Our method account 75.96% higher accidentals than overall smoothing, 13.86% from the binary method, and 1.94% from spatially varying, respectively.

Recall that, median percentage ratio, we consider the vector of all the log probabilities for method M denoted as $\{P(Y_s = y_s | C_s, M) : s \in \mathcal{S}\}$. For two methods M_1 and M_2 , we compute the shoe-specific ratios:

$$R_s^{M_1, M_2} = \frac{\exp(m(Y_s = y_s | C_s, M_1))}{\exp(m(Y_s = y_s | C_s, M_2))}, \quad s \in \mathcal{S},$$

and summarize the resulting vector $(R_s^{M_1, M_2})_{s \in \mathcal{S}}$ by its median (Table 7 and Table 8), i.e.

$$(31) \quad \tilde{R}_{M_2}^{M_1} = \text{median}_{s \in \mathcal{S}} R_s^{M_1, M_2}.$$

For each pair of methods, we evaluated the ratio of probabilities for each observation and reported the median of these ratios (Equation 31), scaled by 100 for interpretability. A value much greater than 100 indicates that the method in the row significantly outperforms the method in the column. Table 7 presents the median percentage ratios between models. Our proposed method (M(Final)) consistently outperformed all alternative configurations across median percentage ratios. In particular, it showed substantial gains over the no-contact baseline and the uniform model, highlighting the effectiveness of incorporating spatially-informed, multi-level modeling in capturing complex signal structures.

Methods	No contact; overall smoothing (M(a))	Binary contact surface (M(b))	Spatially varying (M(variant A))	Our method (M(Final))	Uniform metric
M(a)	1.0×10^2	2.3×10^{-2}	3.8×10^{-3}	2.3×10^{-3}	6.1×10^6
M(b)	4.4×10^5	1.0×10^2	1.9×10^1	1.3×10^1	1.5×10^{11}
M(variant A)	2.6×10^6	5.2×10^2	1.0×10^2	6.5×10^1	1.7×10^{12}
M(Final)	4.4×10^6	7.7×10^2	1.5×10^2	1.0×10^2	2.7×10^{12}
Uniform metric	1.6×10^{-3}	6.5×10^{-8}	6.0×10^{-9}	3.7×10^{-9}	1.0×10^2

TABLE 7

Median percentage ratios between methods ($\tilde{R}_{M_2}^{M_1}$, Equation 31), where the row method (M_1) is compared to the column method (M_2). We computed the median percentage ratios between methods using exponentiated log-probabilities on a per-shoe basis. For each pair of methods, we evaluated the ratio of probabilities for each observation and reported the median of these ratios, scaled by 100 for interpretability. A value much greater than 100 indicates that the method in the row significantly outperforms the method in the column.

Table 8 presents the median percentage ratios between these variants, which are different spatially varying (SV) modeling strategies. The first four methods—Our method (M(Final));

Methods (including 2^6 fixed effects)	Our method (M(Final))	Intercept, IG and PI; SV (M(variant D))	intercept, PI; SV (M(variant C))	Overall smoothing (only intercept SV) (M(variant B))	intercept, 15 SV (M(variant A))
M(Final)	1.00×10^2	1.01×10^2	1.00×10^2	1.00×10^2	1.54×10^2
M(variant D)	9.94×10^1	1.00×10^2	1.00×10^2	1.01×10^2	1.53×10^2
M(variant C)	9.98×10^1	9.98×10^1	1.00×10^2	1.00×10^2	1.50×10^2
M(variant B)	9.98×10^1	9.94×10^1	9.97×10^1	1.00×10^2	1.48×10^2
M(variant A)	6.48×10^1	6.55×10^1	6.65×10^1	6.73×10^1	1.00×10^2

TABLE 8

Median percentage ratios ($\tilde{R}_{M_1}^{M_2}$, Equation 31) between spatial varying methods, where the row method (M_1) is compared to the column method (M_2). For M(Final)/Our Method (3 SV; pixel intensity, image gradient, and their interaction, with intercept SV); M(variant D)/Only image gradient and pixel intensity as SV with intercept SV; M(variant C) intercept and PI as SV; M(variant B)/Only intercept SV (overall smoothing); and M(variant A)/15 SV (first two order of interactions with 5 covariates excluding image gradient) with intercept SV across ten folds. The first 4 methods have image gradient as a fixed effect (2^6), and the fifth model has no image gradient in fixed effect.

Intercept, image gradient (IG) and pixel intensity (PI) as spatially varying (M(variant D)); Intercept, pixel intensity as spatially varying (M(variant C)); and Overall smoothing with only intercept spatially varying (M(variant B))—show highly comparable performance, with median ratios differing by only a few percent. Importantly, all these approaches include image gradient as a fixed effect along with 2^6 fixed effects, underscoring its consistent value in the model. In contrast, the Intercept, 15 SV model, which omits image gradient from the fixed effects and includes a broader but potentially noisier set of SV terms, demonstrates notably lower performance. This highlights the relevance of targeted covariate inclusion—specifically, image gradient—in improving model fit and predictive quality. Thus, it justifies that our proposed model performed superior among additional variants of our models (M(Variant A), M(Variant B), M(Variant C), and M(Variant D)).

Methods	Our method (M(Final))	15 SV (M(variant A))	Binary contact surface (M(b))	No contact; overall smoothing (M(a))
M(Final)	1.00	0.96 [0.96, 0.97]	0.76 [0.73, 0.78]	0.13 [0.11, 0.15]
M(variant A)	0.96 [0.96, 0.97]	1.00	0.76 [0.74, 0.79]	0.15 [0.12, 0.17]
M(b)	0.76 [0.73, 0.78]	0.76 [0.74, 0.79]	1.00	0.17 [0.15, 0.20]
M(a)	0.13 [0.11, 0.15]	0.15 [0.12, 0.17]	0.17 [0.15, 0.20]	1.00

TABLE 9

Concordance correlation coefficients with 95% confidence intervals between model configurations. [Lawrence and Lin \(1992\)](#), used CCC package from [Desktols](#).

The Concordance Correlation Coefficients (CCCs, [Lawrence and Lin \(1992\)](#)) jointly measure precision through the Pearson correlation and accuracy through penalization of location and scale differences, with values close to one indicating strong agreement between two methods $p_{M_1} := \{m(Y_s = y_s | C_s, M_1) : s \in \mathcal{S}\}$ and $p_{M_2} := \{m(Y_s = y_s | C_s, M_2) : s \in \mathcal{S}\}$ (see appendix, section 1.4). Table 9 presents pairwise CCC with 95% confidence intervals between different model configurations. Our method shows the highest agreement with the 15 SV model (CCC = 0.96), indicating similar predictive performance. Moderate agreement is observed with the binary contact surface model (CCC = 0.76), while the no-contact smoothing baseline shows minimal concordance with all other methods (CCC < 0.17), highlighting the added value of contact-based features.

14. Additional plots

The heatmap of the spatially varying coefficients of pixel intensity, image gradient and their interactions are provided in Figure 11 given a contact surface value of a shoe print (202-L in

WVU database, $x_{s',a}^i(\beta_{sv}^i + \beta_f^i)$, for $i = i_2, i_3$, and i_1). To observe the results separately across each fold, a detailed comparison across ten folds is provided in Figure 13.

Uncertainty quantification in a linear model and generalized linear model framework is popular in scientific problems (Cressie and Wikle (2011), Manna and Ghosh (2025), Manna et al. (2025), Manna, Mehan and Amatya (2024), e.t.c). For a specific fold, please do consider the Figure 12, where we also incorporate the spatially varying coefficients, which incorporate first and second order interactions as spatially varying with all 32 fixed effects but omit any image gradient. A magenta-colored line represents this curve and tends to lie between the binary method (black line) and our method (green line).

A performance comparison based on the described metric for selected methods for all folds in cross-validation is provided in Figure 15.

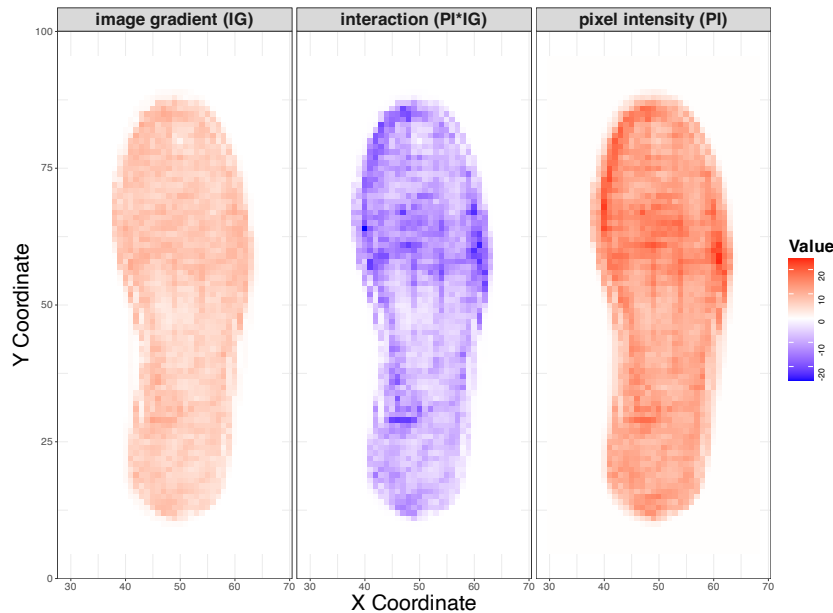


Fig 11: Heatmap for 3 spatially varying coefficients combined with fixed effect for M(Final).

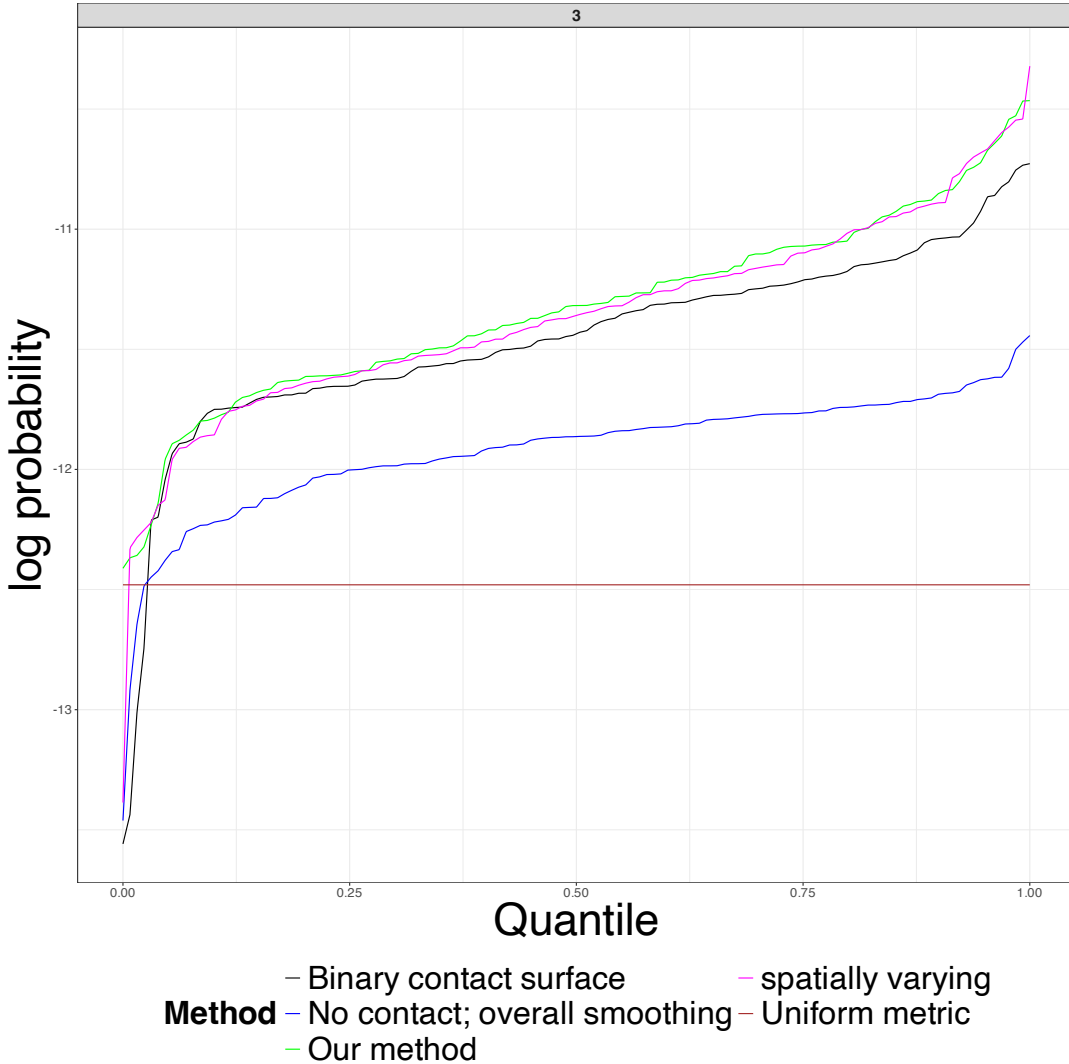


Fig 12: The state-of-the-art comparison of quantiles for different folds.

Note: 1 This plot is made for the robustness check of our method. Although two other existing methods (overall smoothing and binary contact surface; blue and black colored) are crossing below the uniform metric (red), our method (green) turns to be above of other three methods even for lower quantiles across all the folds. We are demonstrating for third fold. The light blue is for the spatially varying method, which incorporates first and second order interactions as spatially varying with all 32 fixed effects but omits any image gradient. This method is in between the final proposed "our method" and the binary. It also reflects the importance of inclusion of the image gradient in our modeling framework.

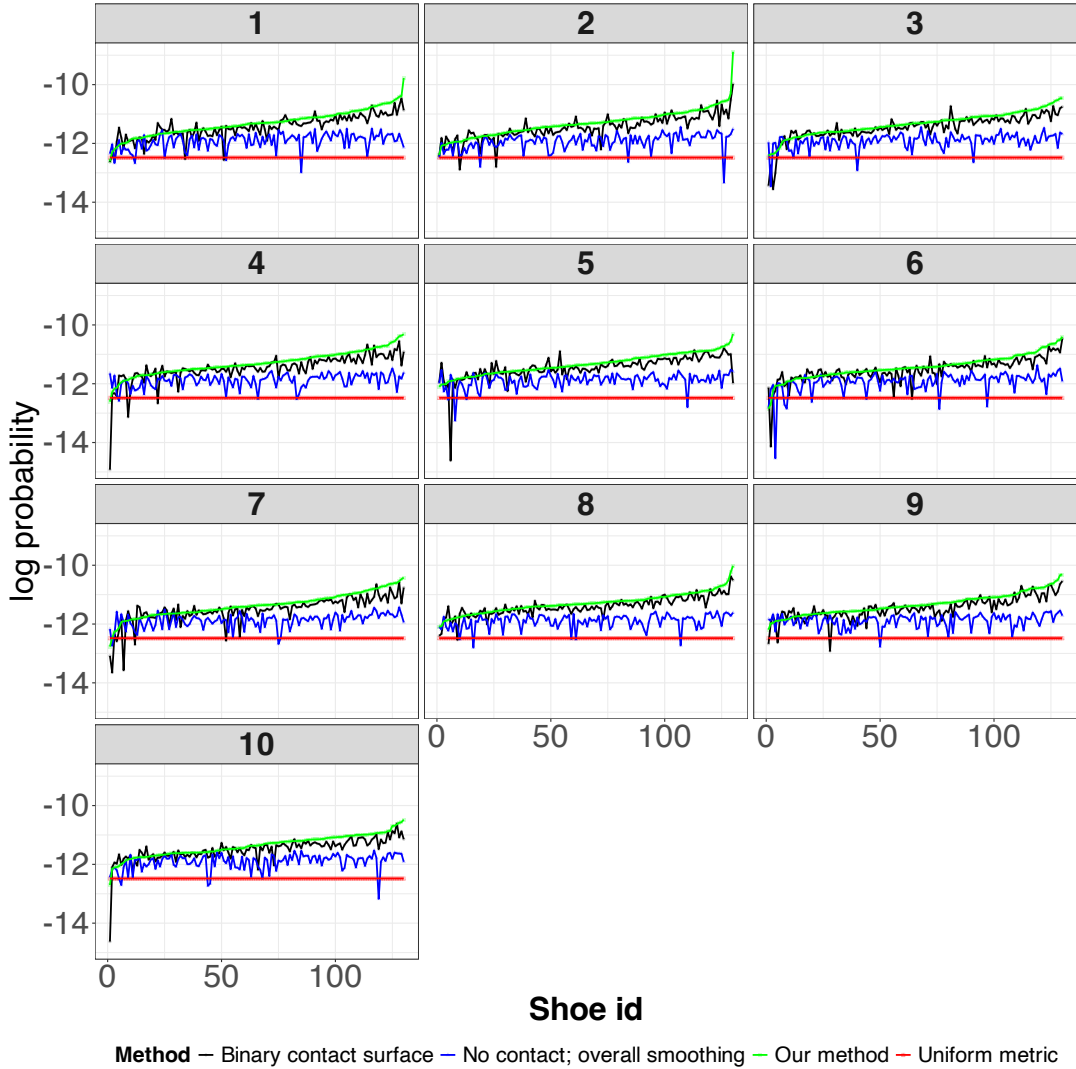


Fig 13: The state-of-the-art comparison and development of performance across different methods for 10 folds.

Note: In the X axis the shoe id is arranged based on the performance of our method, which consists the spatial varying coefficients method with image gradient. Uniform metric (Stone (2006)) and No contact; overall smoothing (Yekutieli et al. (2012)) are two methods that do not incorporate any spatial covariates. Based on the binary contact surface with 32 covariates (Spencer and Murray (2020)) and spatial smoothing the performance was significantly better than methods that do not incorporate any spatial covariate. Finally, our proposed method performed best among all existing methods that incorporate spatial varying coefficients (2^6 fixed effects, overall smoothing, and only 3 random effects i.e. pixel intensity, image gradient, and their interaction) with continuous surfaces. All the methods are arranged based on the performance across our method.

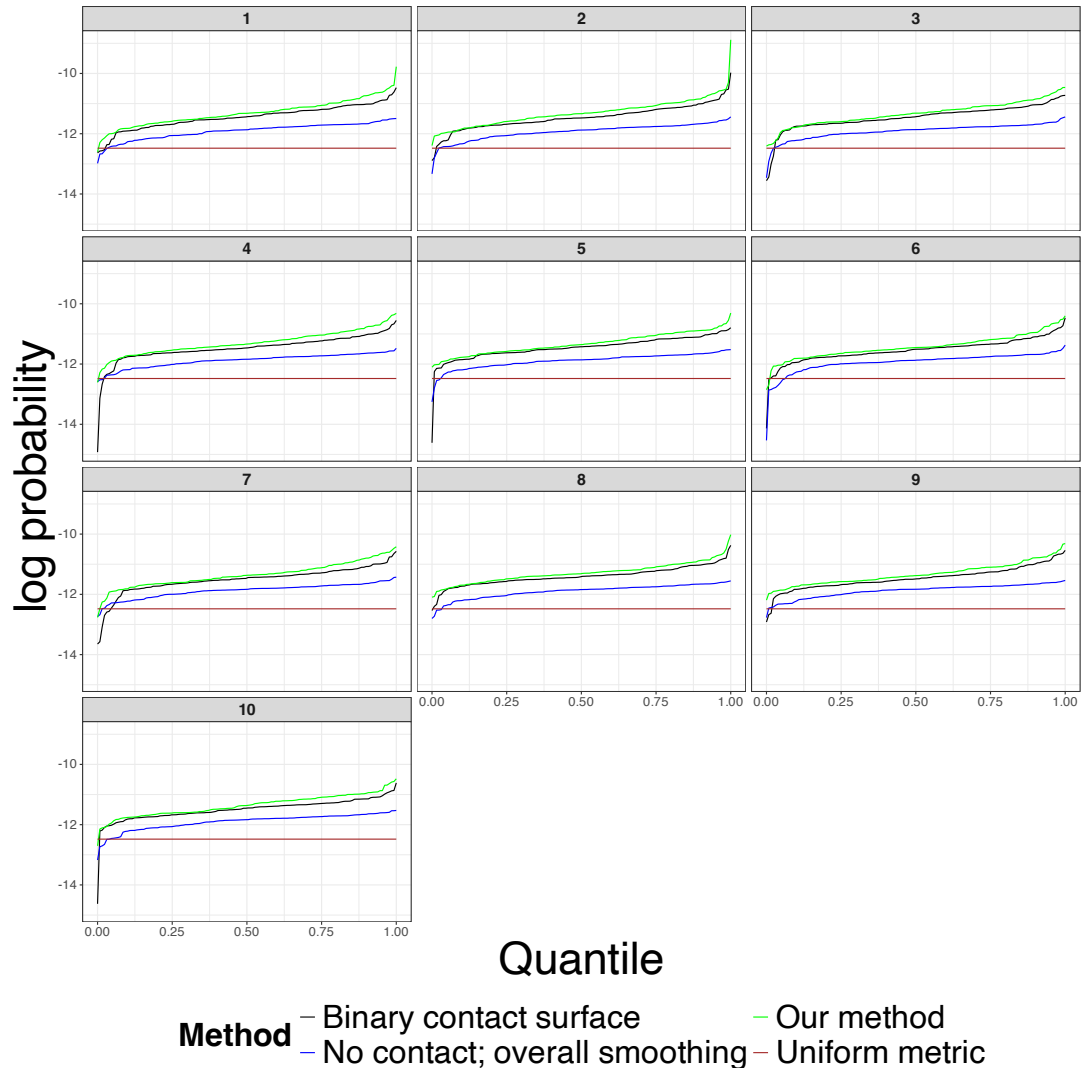


Fig 14: The state-of-the-art comparison of quantiles for different folds.

Note: 1 This plot is made for the robustness check of our method. Although two other existing methods (overall smoothing and binary contact surface; blue and black colored) are crossing below the uniform metric (red), our method (green) turns to be above of other three methods even for lower quantiles across all the folds.

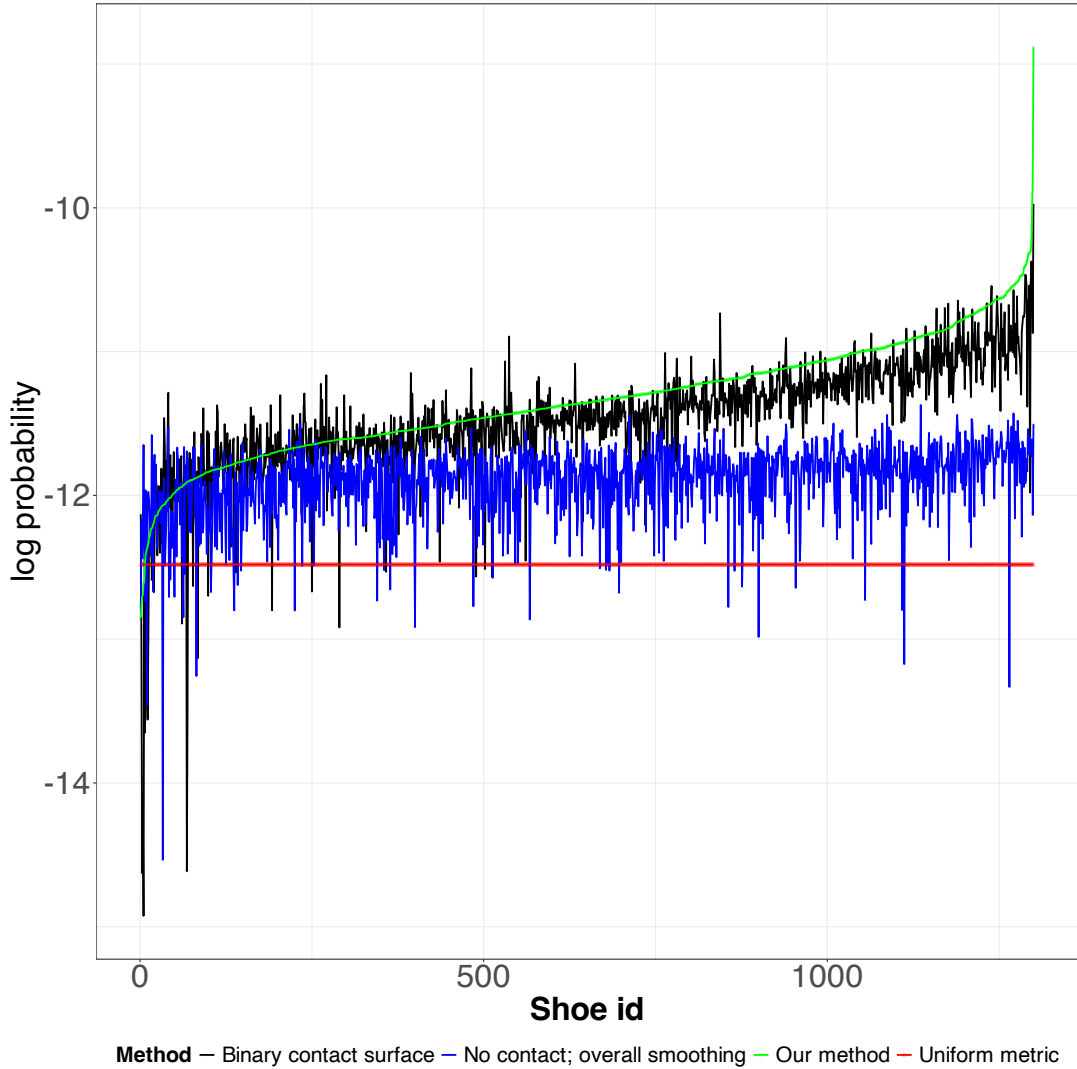


Fig 15: The state-of-the-art comparison and development of performance across different methods for third fold.

Note: In the X axis the shoe id is arranged based on the performance of our method which consists the spatial varying coefficients method with image gradient. Uniform metric (Stone (2006)) and No contact; overall smoothing (Yekutieli et al. (2012)) are two methods that do not incorporate any spatial covariates. Based on the binary contact surface with 32 covariates (Spencer and Murray (2020)) and spatial smoothing the performance was significantly better than methods that do not incorporate any spatial covariate. Finally, our proposed method performed best among all existing methods that incorporate spatial varying coefficients (2^6 fixed effects, overall smoothing, and only 3 random effects i.e. pixel intensity, image gradient, and their interaction) with continuous surfaces. All the methods are arranged based on the performance across our method.

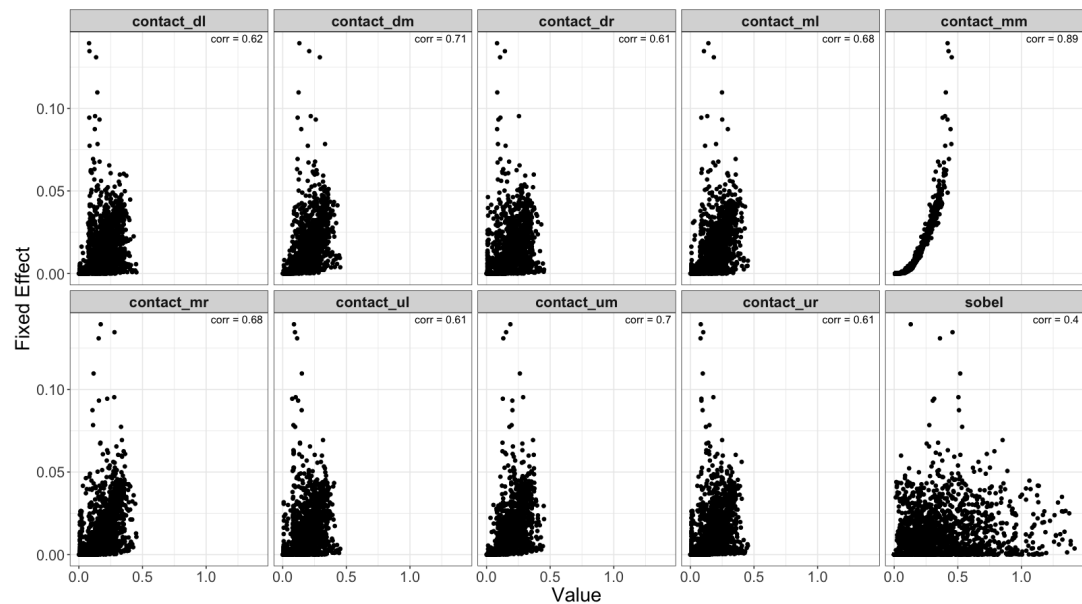


Fig 16: Contact surface, neighborhood, and image gradient versus fixed effect. The contact value (contact_mm) has the highest correlation with the fixed effect of test shoe 4-L. The suffixes _dl, _dm, _dr, _ml, _mr, _ul, _um, _ur correspond to the 8 neighbors of _mm, where m = middle, u = up, d = down, r = right, l = left.

REFERENCES

ADAIR, T., LEMAY, J., McDONALD, A., SHAW, R. and TEWES, R. (2007). The Mount Bierstadt study: An experiment in unique damage formation in footwear. *Journal of Forensic Identification* **57** 199.

BESAG, J. (1974). Spatial interaction and the statistical analysis of lattice systems. *Journal of the Royal Statistical Society: Series B (Methodological)* **36** 192–225.

BLANGIARDO, M., CAMELETTI, M., BAIO, G. and RUE, H. (2013). Spatial and spatio-temporal models with R-INLA. *Spatial and spatio-temporal epidemiology* **7** 39–55.

BODZIAK, W. J. (2017). *Footwear impression evidence: detection, recovery and examination*. CRC Press.

CHAMPOD, C., VOISARD, R. and GIROD, A. (2000). A statistical study of air bubbles on athletic shoesoles. *Forensic science international* **109** 105–123.

CHOCHÓŁ, A. and ŚWIĘTEK, M. (2012). Characteristics of forensic shoe sole databases. *Problems of Forensic Sciences* **1** 164–177.

COUNCIL, N. R., ON ENGINEERING, D., SCIENCES, P., ON APPLIED, C., STATISTICS, T., AFFAIRS, G., ON SCIENCE, C., LAW and ON IDENTIFYING THE NEEDS OF THE FORENSIC SCIENCES COMMUNITY, C. (2009). *Strengthening forensic science in the United States: a path forward*. National Academies Press.

CRESSIE, N. and WIKLE, C. K. (2011). *Statistics for spatio-temporal data*. John Wiley & Sons.

DAMARY, N. K., MANDEL, M., WIESNER, S., YEKUTIELI, Y., SHOR, Y. and SPIEGELMAN, C. (2018). Dependence among randomly acquired characteristics on shoeprints and their features. *Forensic science international* **283** 173–179.

DAMARY, N. K., MANDEL, M., YEKUTIELI, Y., WIESNER, S. and SHOR, Y. (2019). Spatial modeling of randomly acquired characteristics on outsoles with application to forensic shoeprint analysis. *arXiv preprint arXiv:1912.08272*.

EVETT, I., LAMBERT, J. and BUCKLETON, J. (1998). A Bayesian approach to interpreting footwear marks in forensic casework. *Science & Justice* **38** 241–247.

FRUCHTENICHT, T., HERZIG, W. and BLACKLEDGE, R. D. (2002). The discrimination of two-dimensional military boot impressions based on wear patterns. *Science & justice* **42** 97–104.

HASTIE, T. and TIBSHIRANI, R. (1986). Generalized additive models. *Statistical science* **1** 297–310.

HOLDREN, J., LANDER, E., PRESS, W., SAVITZ, M., AUSTIN, W., CHYBA, C. et al. (2016). Report to the president forensic science in criminal courts: Ensuring scientific validity of feature-comparison methods. *Subcommittee on the Social and Behavioral Sciences Team: United States Government*.

JANG, M., CARRIQUIRY, A. and PARK, S. (2025). Enhancing forensic shoeprint analysis: Application of the Shoe-MS algorithm to challenging evidence. *Science & Justice* 101255.

JANG, M., PARK, S. and CARRIQUIRY, A. (2023). A finely tuned deep transfer learning algorithm to compare outsole images. *Statistical Analysis and Data Mining: The ASA Data Science Journal* **16** 511–527.

KAPLAN-DAMARY, N., MANDEL, M., YEKUTIELI, Y., SHOR, Y. and WIESNER, S. (2022). Location distribution of randomly acquired characteristics on a shoe sole. *Journal of Forensic Sciences* **67** 1801–1809.

KEEFE, M. J., FERREIRA, M. A. and FRANCK, C. T. (2018). On the formal specification of sum-zero constrained intrinsic conditional autoregressive models. *Spatial statistics* **24** 54–65.

KINGMAN, J. F. C. (1993). *Poisson Processes. Oxford Studies in Probability* **3**. Oxford University Press, Oxford.

KONG, B., SUPANCIC, J., RAMANAN, D. and FOWLKES, C. (2017). Cross-domain forensic shoeprint matching. *British Machine Vision Conference (BMVC)*.

KORTYLEWSKI, A., ALBRECHT, T. and VETTER, T. (2014). Unsupervised footwear impression analysis and retrieval from crime scene data. In *Asian conference on computer vision* 644–658. Springer.

LAWRENCE, I. and LIN, K. (1992). Assay validation using the concordance correlation coefficient. *Biometrics* 599–604.

LIN, E.-T., DEBAT, T. and SPEIR, J. A. (2022). A simulated crime scene footwear impression database for teaching and research purposes. *Journal of Forensic Sciences* **67** 726–734.

LUND, S. P. and IYER, H. (2016). Likelihood ratio as weight of forensic evidence: A metrological perspective. *arXiv preprint arXiv:1608.07598*.

LUND, S. P. and IYER, H. (2017). Likelihood ratio as weight of forensic evidence: a closer look. *Journal of Research of the National Institute of Standards and Technology* **122** 1.

LUND, S. and IYER, H. (2022). Bayesian Reasoning and Evidence Communication. *arXiv preprint arXiv:2205.04677*.

MANNA, A. and GHOSH, S. K. (2025). Bayesian Models for Joint Selection of Features and Auto-Regressive Lags: Theory and Applications in Environmental and Financial Forecasting. *arXiv preprint arXiv:2508.10055*.

MANNA, A., MEHAN, S. and AMATYA, D. M. (2024). Development of a Statistical Predictive Model for Daily Water Table Depth and Important Variables Selection for Inference. *arXiv preprint arXiv:2410.01001*.

MANNA, A., VIKRAM SETT, A., DEY, D. K., GU, Y., SCHIFANO, E. D. and HE, J. (2025). Conformal Prediction Inference in Regularized Insurance Models. *Applied Stochastic Models in Business and Industry* **41** e70045.

MARTINO, S., AKERKAR, R. and RUE, H. (2011). Approximate Bayesian inference for survival models. *Scandinavian Journal of Statistics* **38** 514–528.

PASQUIER, J. (2023). A footwear marks database in Western Switzerland: A forensic intelligence success. *Forensic Science International* **348** 111726.

PAU, G., FUCHS, F., SKLYAR, O., BOUTROS, M. and HUBER, W. (2010). EBImage—an R package for image processing with applications to cellular phenotypes. *Bioinformatics* **26** 979–981.

PERPEROGLOU, A., SAUERBREI, W., ABRAHAMOWICZ, M. and SCHMID, M. (2019). A review of spline function procedures in R. *BMC medical research methodology* **19** 1–16.

RICHETELLI, N., BODZIAK, W. J. and SPEIR, J. A. (2019). Empirically observed and predicted estimates of chance association: Estimating the chance association of randomly acquired characteristics in footwear comparisons. *Forensic science international* **302** 109833.

RICHETELLI, N. and SPEIR, J. A. (2022). Spatial frequency of randomly acquired characteristics on outsoles. *Journal of Forensic Sciences* **67** 1810–1824.

RICHETELLI, N., NOBEL, M., BODZIAK, W. J. and SPEIR, J. A. (2017). Quantitative assessment of similarity between randomly acquired characteristics on high quality exemplars and crime scene impressions via analysis of feature size and shape. *Forensic Science International* **270** 211–222.

RUE, H., MARTINO, S. and CHOPIN, N. (2009). Approximate Bayesian inference for latent Gaussian models by using integrated nested Laplace approximations. *Journal of the Royal Statistical Society Series B: Statistical Methodology* **71** 319–392.

RUE, H., RIEBLER, A., SØRBYE, S. H., ILLIAN, J. B., SIMPSON, D. P. and LINDGREN, F. K. (2017). Bayesian computing with INLA: a review. *Annual Review of Statistics and Its Application* **4** 395–421.

RUE, H., LINDGREN, F., SIMPSON, D., ILLIAN, J., SØRBYE, S. and RIEBLER, A. (2024). R-INLA: Approximate Bayesian inference using INLA. R package.

SHAFIQUE, S., KONG, B., KONG, S. and FOWLKES, C. (2023). Creating a forensic database of shoeprints from online shoe-tread photos. In *Proceedings of the IEEE/CVF Winter Conference on Applications of Computer Vision* 858–868.

SHOR, Y., WIESNER, S., TSACH, T., GUREL, R. and YEKUTIELI, Y. (2018). Inherent variation in multiple shoe-sole test impressions. *Forensic Science International* **285** 189–203.

SIMPSON, D., ILLIAN, J. B., LINDGREN, F., SØRBYE, S. H. and RUE, H. (2016). Going off grid: computationally efficient inference for log-Gaussian Cox processes. *Biometrika* **103** 49–70.

SKERRETT, J., NEUMANN, C. and MATEOS-GARCIA, I. (2011). A Bayesian approach for interpreting shoemark evidence in forensic casework: Accounting for wear features. *Forensic Science International* **210** 26–30.

SMALE, A. N. and SPEIR, J. A. (2023). Estimate of the random match frequency of acquired characteristics in a forensic footwear database. *Science & Justice* **63** 427–437.

SMALE, A. N. and SPEIR, J. A. (2024a). Estimate of the random match frequency of acquired characteristics in footwear: Part I—Impressions in blood. *Science & justice* **64** 117–133.

SMALE, A. N. and SPEIR, J. A. (2024b). Estimate of the random match frequency of acquired characteristics in footwear: Part II—Impressions in dust. *Science & Justice* **64** 134–150.

SPEIR, J. A., RICHETELLI, N., FAGERT, M., HITE, M. and BODZIAK, W. J. (2016). Quantifying randomly acquired characteristics on outsoles in terms of shape and position. *Forensic science international* **266** 399–411.

SPENCER, N. A. and MURRAY, J. S. (2020). A Bayesian hierarchical model for evaluating forensic footwear evidence. *The Annals of Applied Statistics* **14** 1449–1470.

SRIHARI, S. N. (2011). Analysis of footwear impression evidence. *US DoJ Report*.

SRIHARI, S. N. and TANG, Y. (2014). Computational methods for the analysis of footwear impression evidence. In *Computational Intelligence in Digital Forensics: Forensic Investigation and Applications* 333–383. Springer.

STONE, R. S. (2006). Footwear examinations: Mathematical probabilities of theoretical individual characteristics. *Journal of Forensic Identification* **56** 577.

VENKATASUBRAMANIAN, G., HEGDE, V., PADI, S., IYER, H. and HERMAN, M. (2021). Comparing footwear impressions that are close non-matches using correlation-based approaches. *Journal of Forensic Sciences* **66** 890–909.

VETTERLI, M., NUSSBAUMER, H. J. et al. (1984). Simple FFT and DCT algorithms with reduced number of operations. *Signal processing* **6** 267–278.

WANG, Y., DEGLERIS, A., WILLIAMS, A. and LINDERMAN, S. W. (2024). Spatiotemporal clustering with Neyman-Scott processes via connections to Bayesian nonparametric mixture models. *Journal of the American Statistical Association* **119** 2382–2395.

WIESNER, S., SHOR, Y., TSACH, T., KAPLAN-DAMARY, N. and YEKUTIELI, Y. (2020). Dataset of digitized RACs and their rarity score analysis for strengthening shoeprint evidence. *Journal of forensic sciences* **65** 762–774.

WILSON, H. D. (2012). Comparison of the Individual Characteristics in the Outsoles of Thirty-Nine Pairs of Adidas Supernova Classic Shoes. *Journal of Forensic Identification* **62**.

YEKUTIELI, Y., SHOR, Y., WIESNER, S. and TSACH, T. (2012). Expert assisting computerized system for evaluating the degree of certainty in 2d shoeprints. *The US Department of Justice: Washington, DC, USA*.